Journal Pre-proof

Noise radiated from a periodically stiffened cylindrical shell excited by a turbulent boundary layer

Laurent Maxit, Oriol Guasch, Valentin Meyer, Mahmoud Karimi

Please cite this article as: L. Maxit, O. Guasch, V. Meyer, M. Karimi, Noise radiated from a periodically stiffened cylindrical shell excited by a turbulent boundary layer, *Journal of Sound and Vibration* (2019), doi: https://doi.org/10.1016/j.jsv.2019.115016.

This is a PDF file of an article that has undergone enhancements after acceptance, such as the addition of a cover page and metadata, and formatting for readability, but it is not yet the definitive version of record. This version will undergo additional copyediting, typesetting and review before it is published in its final form, but we are providing this version to give early visibility of the article. Please note that, during the production process, errors may be discovered which could affect the content, and all legal disclaimers that apply to the journal pertain.

Noise radiated from a periodically stiffened cylindrical shell excited by a turbulent boundary layer

Laurent Maxit[1], Oriol Guasch[2], Valentin Meyer[3], Mahmoud Karimi[4]

1. Univ Lyon, INSA–Lyon, Laboratoire Vibrations-Acoustique (LVA), 25 bis, av. Jean Capelle, F-69621, Villeurbanne Cedex, France.

    e-mail: laurent.maxit@insa-lyon.fr (corresponding author)

2. GTM - Grup de recerca en Tecnologies Mèdia, La Salle, Universitat Ramon Llull, C/ Quatre Camins 30, 08022 Barcelona, Catalonia, Spain.

3. Naval Group Research, 199 avenue Pierre-Gilles, 83190 Ollioules, France

4. Centre for Audio, Acoustics and Vibration, University of Technology Sydney, Sydney, Australia

Abstract

This work proposes a semi-analytical method to model the vibroacoustic behavior of submerged cylindrical shells periodically stiffened by axisymmetric frames and excited by a homogeneous and fully developed turbulent boundary layer (TBL). The process requires the computation of the TBL wall-pressure cross spectral density function and the sensitivity functions for stiffened cylindrical shells. The former is deduced from an existent TBL model and the latter are derived from a wavenumber-point reciprocity principle and a spectral formulation of the problem. The stiffeners' dynamic behavior is introduced in the formulation through circumferential admittances that are computed by a standard finite element code using shell elements. Four degrees of freedom are taken into account for the coupling between the shell and the stiffeners: three translation directions and one tangential rotation. To investigate the effect of the stiffeners on the radiated noise, two case studies are considered. The first one examines a fluid-loaded cylindrical shell with regularly spaced simple supports. The influence of Bloch-Floquet waves and the support spacing on the noise radiation are highlighted. The second case study inspects the fluid-loaded cylindrical shell with two different periodic ring stiffeners, namely stiffeners with T-shaped and I-shaped cross-sections. Their influence on the vibroacoustics of the shell is thoroughly analyzed.

Keywords: stiffened cylindrical shell; turbulent boundary layer; fluid loading; noise prediction; Bloch-Floquet wave;

1. Introduction

Stiffened structures excited by a turbulent boundary layer (TBL) are found in many vehicles such as aircrafts, trains, and submarines. Predicting the noise and vibrations they generate is very important at the design stage, as well as for optimization and refinement of the products. In naval applications, for example, a submarine hull can be modelled as a stiffened cylindrical shell. In order to control the radiated noise from a submarine, it is therefore important to understand how a stiffened cylindrical shell reacts to TBL excitation. This paper proposes the modelling of an infinite periodically stiffened cylindrical shell immersed in a heavy fluid (i.e. water) and excited by a homogeneous and fully developed TBL. The model will allow engineers to investigate the effect of the periodicity of the stiffeners and their influence on the shell vibroacoustics. This study is thus multidisciplinary and includes the vibration analysis of periodically stiffened cylindrical structures, as well as the prediction of the radiated noise under the excitation of a partially correlated pressure field.

The dynamic response and the sound radiation from periodically stiffened structures have been addressed by many authors. Before reviewing the extensive state of the art on the topic, however, let us briefly introduce which will be the main new contributions of this work to the field. On the one hand, we are proposing a semi-analytical method to characterize the vibroacoustic response of a periodically stiffened cylindrical shell excited by a TBL. The suggested formulation has not been attempted before, to the best of our knowledge, and it presents some singular features. First, it is based on an original reciprocity principle, which allows us to identify the so-called sensitivity functions of the structure. Those are computed considering four degrees of freedom (DoF) in the coupling between the shell and the stiffeners, namely three translations and a tangential rotation, while previous works only assumed one DoF along the radial direction. Moreover, in the current approach the stiffeners are represented by admittances calculated with the finite element method, which allows one to describe the deformation of the stiffener cross sections, contrary to what occurs in the beam-like models generally adopted in literature. All results in a more realistic modelling of periodically stiffened shells. In addition, the current study reveals the bumps observed in the spectra of the far-field radiated pressure can be directly attributed to the propagation of Bloch-Floquet waves in the periodically stiffened shell.

As said before, the study of periodically stiffened structures has now a long history. Mead [1] analyzed the free wave propagation in an infinite periodically supported beam using the so-called space-harmonic method. He showed that the vibration energy can propagate only in certain frequency bands. Outside these bands, the waves decay strongly with the distance along the beam, and the energy cannot propagate. Subsequently, Rumerman [2] proposed a mathematical formulation for wave propagation and forced vibration of periodically stiffened infinite plates. Assuming plane wave excitation, he was able to obtain an explicit solution. The principle of superposition was then used to construct the solution for an arbitrary excitation. A similar approach was employed by Mace [3] to investigate the vibrations of an infinite periodically stiffened fluid-loaded plate excited by convective harmonic pressure. He demonstrated that the propagating wave, corresponding to the near field wave in an unstiffened plate, was damped by acoustic radiation. The results showed that the responses to a convected harmonic pressure and the far field directivity contain peaks at certain frequencies and angles, which were attributed to the free wave propagation characteristics of the fluid-loaded plate.

Among the intensive research carried out on the wave propagation in continuous periodic structures at the University of Southampton (see the review paper in [4]), Mead also studied the radiation of regularly stiffened plates [5]. He employed the space-harmonic approach for the prediction of the structural and acoustic response of the periodically stiffened plate, taking the fluid-loading effects into account. Plates stiffened in one or two orthogonal directions were considered. It was shown that five space harmonics in each spatial direction are enough to predict the peaks of the radiated sound power spectrum.

Lee and Kim [6] developed an exact solution procedure to calculate the sound transmission through an infinitely long elastic panel stiffened only in one direction. The stiffener was modelled as a set of lumped masses attached to the panel. The dynamic equation was derived using the space harmonic approach and the virtual energy principle. It was shown that the wave reflection produced by the stiffeners changed the dispersion relationship and caused the panel to be excited in a coincidental manner by incident sound waves, at frequencies below the critical frequency. Additionally, Yuan et al [7] numerically and experimentally studied the vibroacoustic response of a fluid-loaded, simply supported rectangular plate covered by a composite acoustic coating. They found that only when the loss modulus of the damping layer was sufficiently high and the

3

stiffness of the decoupling layer was sufficiently low, the system can provide an excellent vibration isolation and noise reduction effect. Likewise, Fu et al. [8] developed an analytical model to investigate the sound transmission loss from an orthogonally rib-stiffened plate structure under diffuse acoustic field excitation. Numerical results showed that if the effects of the modal coupling terms are neglected, the sound power could be either overestimated or underestimated depending on the frequency range and excitation locations.

As regards cylindrical structures not so many works exist in literature. Mead and Bardell [9] computed the propagation constants of a periodic frame-stiffened cylindrical shell using an exact closed-form solution. They determined the stop and pass-bands of free wave motion in the structure. For the cylinder with solid rectangular-section frames, a narrow frequency band was observed where two distinctly different wave motions can propagate simultaneously. Hodges et al. [10] used the space-harmonic method to present the theory of vibrations of a cylinder braced by circular T-section ribs spaced regularly along its length. A good agreement was obtained between their modelling and measurements on a ribbed cylinder over a frequency range from zero to about three times the ring frequency [11]. It was shown that the first three pass-bands for vibration transmission along the cylinder occurred in this frequency range, associated with the first two resonant modes of a single bay of the structure and with a cross-sectional resonance of the T-section ribs.

Noise emission was addressed by Burroughs [12], who derived analytical expressions for the far-field acoustic radiation from a point-driven circular cylindrical shell reinforced by doubly periodic rings. The rings interacted with the shell only through the radial direction. Radiation from the shell appeared like an array of ring radiators located at the ring support. More recently, Yan et al. [13,14] applied the space-harmonic approach to predict the sound radiation from a submerged periodic ring-stiffened shell excited by a harmonic line force. The stiffeners had uniform rectangular section and they could interact with the shell along four degrees of freedom (i.e. three translations and one tangential rotation). It was found that characteristics of the vibrational power flow propagation vary with different circumferential mode orders and frequencies. For the circumferential mode order n = 0, the power flow in the shell wall was predominantly carried by the motion in the axial direction.

The vibration of an infinitely long cylindrical shell with internal periodic lengthwise ribs was analytically formulated by Tong et al. [15]. The lengthwise rib was modeled as an

elastic beam with longitudinal and flexural motions. A circumferential mode expansion was employed to obtain the shell motion using periodicity in the circumferential direction and the Fourier transform in the longitudinal direction. It was demonstrated that the acoustic radiation resonances in the far field are due to the supersonic components of the radiated flexural Bloch waves. Cao et al. [16] studied the acoustic radiation from shear deformable stiffened laminated cylindrical shells excited by a radial point force. Initial axial loadings and double periodic rings were considered. The mathematical problem was based on the use of the space Fourier transform and the Poisson summation formula. The pressure radiated in the far field was estimated using the phase-stationary theorem. It was pointed out that the shear deformation of the rings cannot be neglected in the high frequency range. Cao et al.'s work was extended by Tang et al. [17] to investigate acoustic radiation from a point driven, infinite, and periodically ring-stiffened shell, in the presence of mean flow. To obtain more accurate results, both the effects of in-plane and out-of-plane vibrations of the ring-stiffeners on the radial displacement of the shell were taken into account. It was demonstrated that the effects of the Mach number on the sound pressure radiated by the shell were not significant as the Mach number was not greater than 0.02.

As reviewed above, many researchers have studied the dynamical behavior of stiffened structures. However, only few studies focused on stiffened structures excited by TBLs (see for example, [18,19]). In this line, Rumerman [20] derived expressions for the broadband estimation of the acoustic power radiated from a finite ribbed plate excited by a TBL. The response was directly formulated in terms of acoustic power, and the effects of the supports were taken into account using power scattering coefficients, which were calculated through a Wiener–Hopf analysis. Maxit et al. [21] developed a methodology for estimating the vibro-acoustic response of a periodically stiffened plate excited by a TBL, from the knowledge of the wall pressure spectrum induced by the TBL and from the sensitivity functions of the panel. The latter included the responses of the panel to unit convected harmonic pressure waves, which can be estimated from a wavenumber-point reciprocity principle [21-24]. The computational process to estimate the stiffened panel response to TBL excitation is then reduced to a numerical integration of a product of two analytical quantities, the first one is the wall pressure spectrum and the second one is the square of the absolute value of the sensitivity functions.

In this work, a similar approach has been employed to study the noise radiated by a cylindrical shell periodically stiffened by axisymmetric frames and excited by a homogeneous and fully developed TBL. In addition to modelling a fluid-loaded

cylindrical shell instead of a fluid-loaded plate, the present case exhibits two challenges. First, in the previous study for the stiffened flat plate [21], the stiffeners were modelled by torsional and flexural beam models. This could be valid for straight stiffeners and for low frequencies. However, it is not valid for modelling ring stiffeners. In the present study, axisymmetric frames with arbitrary cross-section have been considered. Their dynamic behaviors have been characterized by a finite element model based on shell elements [25]. In particular, the deformation of the cross-section could be described as well as the coupling between the different types of motions due to the curvature of the stiffener. Second, the rigid coupling between the shell and the frames need to be defined about the four relevant DoF, instead of considering only the couplings with two DoF (i.e. the normal translation and the torsional rotation). For a flat-plate model, the in-plane and the flexural motions are not coupled together and it is well justified to consider only the two DoF related to the flexural motions. However, for a cylindrical shell the in-plane and flexural motions can be coupled together, in particular below the ring frequency. Therefore, to correctly describe the interaction between the shell and the stiffeners, the four DoF need to be considered.

This paper is divided in two sections. Section 2 contains all theoretical developments. It first describes the wavenumber-frequency formulation of the radiated pressure by the cylindrical shell excited by a random pressure field. The wavenumber-point reciprocity technique is then introduced to facilitate the evaluation of the quantities characterizing the immersed stiffened shell in this formalism. A model for the periodically stiffened cylindrical shell loaded by a fluid in the wavenumber space is worked out. The section finishes with some considerations concerning practical implementation aspects of the method. Section 3 focuses on a thorough analysis of the physics behind noise radiated by an infinite cylindrical shell with periodic simple supports and by a cylindrical shell with periodic stiffeners of rectangular and T-shaped cross sections. Conclusions close the paper in Section 4.

2. Theoretical formulation

2.1 Statement of the problem

Let us consider an infinite cylindrical shell of radius R reinforced by periodic ring stiffeners separated a distance d apart. The shell is immersed in a fluid that moves with

free stream velocity U_0. We assume that a stationary, homogenous, turbulent boundary layer of thickness δ_{tbl} has fully developed on the shell surface. Consequently, the shell vibrates and radiates sound outwards. A general sketch of the situation is depicted in Fig. 1.

It is the main purpose of this work to characterize the sound emitted by the shell. To that goal we have assumed the shell motion and the TBL to be weakly coupled, in the sense that the vibrations of the former do not affect the flow fluctuations beneath the TBL. We have also supposed that the acoustic wave propagation is neither influenced by the TBL nor by the free stream velocity.

The problem can be mathematically described as follows. Consider an arbitrary point M in the flow with cylindrical coordinates (x, θ, r); x standing for the streamwise direction, θ for the azimuthal angle and r for the radial distance. For a given angular frequency, ω, the auto spectral density (ASD) of the radiated acoustic pressure at M, $S_{pp}(x, \theta, r, \omega)$, can be obtained in terms of the TBL wall-pressure cross spectral density (CSD), ϕ_{pp}^{tbl}, and the frequency response function (FRF) of the shell, $H_{p/F}$. Indeed, for a partially space-correlated random excitation, such as the TBL, one can write (see [26] for details),

$$S_{pp}(x, \theta, r, \omega) = \int_{-\infty}^{+\infty} \int_{-\infty}^{+\infty} \int_{0}^{2\pi} \int_{0}^{2\pi} \left| H_{p/F}\left(x, \theta, r, \tilde{x}, \tilde{\theta}, \omega\right) \right|^2 \phi_{pp}^{tbl}\left(\tilde{\tilde{x}} - \tilde{x}, \tilde{\tilde{\theta}} - \tilde{\theta}, \omega\right) R^2 d\tilde{\theta} d\tilde{\tilde{\theta}} d\tilde{x} d\tilde{\tilde{x}}. \qquad (1)$$

The FRF $H_{p/F}\left(x, \theta, r, \tilde{x}, \tilde{\theta}, \omega\right)$ in Eq. (1) provides the acoustic pressure at point $M(x, \theta, r)$ in the fluid, when a unit radial point force is applied at point $\tilde{M}\left(\tilde{x}, \tilde{\theta}, R\right)$ on the shell (see Fig. 1), while ϕ_{pp}^{tbl} characterizes the intense pressure fluctuations beneath the TBL. Solving the integral in Eq. (1) is all what is needed to get the radiated sound pressure field, so the remaining theoretical sections in this work are devoted to finding appropriate expressions for the excitation ϕ_{pp}^{tbl} and the response $H_{p/F}$.

2.2 Turbulent boundary layer on a cylindrical shell

Several models have been proposed in literature to characterize the wall-pressure field (WPF) developed beneath a TBL (see e.g., [27-29]). However, these models are mainly intended for TBLs over flat surfaces. In the spatial domain, they provide the CSD of the wall-pressure, $S_{pp}^{tbl}(x, y, \omega)$, with x and y respectively representing the streamwise and

7

spanwise directions. The CSD for the WPF is also often given in the wavenumber space, $\tilde{S}_{pp}^{tbl}\left(k_x, k_y, \omega\right)$, so that

$$\tilde{S}_{pp}^{tbl}\left(k_x, k_y, \omega\right) = \int\limits_{-\infty}^{+\infty} \int\limits_{-\infty}^{+\infty} S_{pp}^{tbl}\left(x, y, \omega\right) e^{-jk_x x} e^{-jk_y y} dx dy \,, \tag{2}$$

$$S_{pp}^{tbl}\left(x, y, \omega\right) = \frac{1}{\left(2\pi\right)^2} \int\limits_{-\infty}^{+\infty} \int\limits_{-\infty}^{+\infty} \tilde{S}_{pp}^{tbl}\left(k_x, k_y, \omega\right) e^{jk_x x} e^{jk_y y} dk_x dk_y \,. \tag{3}$$

Despite of existent models only being established for TBL over flat areas, our interest is in cylindrical shells for applications in the naval and/or aeronautical sectors. This means that the curvature of the shell will be large in comparison to the TBL thickness (typically around 100 times bigger) and its effects on the TBL models minimal [30]. Therefore, and as carried out in previous studies (see e.g., [31], [32]), we could well adopt flat TBL models for our big cylindrical shells. In fact, the only modification that needs to be made to them is that of imposing a periodicity condition in the spanwise direction. The latter corresponds to the angular position on the shell circumference, so the WPF must be $2\pi R$ periodic along it.

Let us denote by $\tilde{\phi}_{pp}^{tbl}\left(k_x, n, \omega\right)$ the CSD of the WPF in the wavenumber space satisfying the periodicity condition. Here n is an integer that designates a circumferential counter. It is shown in Appendix A, that, from a given TBL model for flat surfaces, $\tilde{S}_{pp}^{tbl}\left(k_x, k_y, \omega\right)$, one can readily obtain its analogous for the shell as

$$\tilde{\phi}_{pp}^{tbl}\left(k_x, n, \omega\right) = \frac{1}{2\pi R} \tilde{S}_{pp}^{tbl}\left(k_x, \frac{n}{R}, \omega\right). \tag{4}$$

The spatial domain counterpart of Eq. (4) is the one to be input in Eq. (1) for computing the radiated acoustic pressure. This can be obtained as (see Appendix A),

$$\phi_{pp}^{tbl}\left(x, \theta, \omega\right) = \frac{1}{2\pi} \sum_{n=-\infty}^{+\infty} \left\{ \int\limits_{-\infty}^{+\infty} \tilde{\phi}_{pp}^{tbl}\left(k_x, n, \omega\right) e^{jk_x x} dk_x \right\} e^{jn\theta} \,. \tag{5}$$

The specific TBL model used for the computations in the current work is of no matter at this point and will be later introduced in Section 2.5.

2.3 Shell frequency response function and the reciprocity principle

The next step to compute the radiated sound pressure in Eq. (1) is that of obtaining a proper expression for the shell FRF. This can be derived from the wavenumber-point reciprocity technique introduced in [21,22], which is based on the wavenumber-frequency

formulation of [21,26]. Let us briefly outline the procedure.

Introducing Eq. (5) into Eq. (1), we get, after some integral manipulations (see [21,26]),

$$S_{pp}(x,\theta,r,\omega) = 2\pi \sum_{n=-\infty}^{n=+\infty} \int_{-\infty}^{+\infty} \left| \tilde{H}_p(x,\theta,r,k_x,n,\omega) \right|^2 \tilde{\phi}_{pp}^{tbl}(k_x,n,\omega) dk_x, \tag{6}$$

where

$$\tilde{H}_p(x,\theta,r,k_x,n,\omega) \equiv \frac{1}{2\pi} \int_{-\infty}^{+\infty} \int_0^{2\pi} H_{p/F}(x,\theta,r,\tilde{x},\tilde{\theta},\omega) e^{-jk_x\tilde{x}} e^{-jn\tilde{\theta}} R d\tilde{\theta} d\tilde{x}. \tag{7}$$

$\tilde{H}_p(x,\theta,r,k_x,n,\omega)$ is called the pressure circumferential sensitivity function at point $M(x,\theta,r)$. As seen from Eq. (7), it determines the acoustic pressure at M when the shell is excited by wall-pressure waves $p(x,\theta) = e^{-j(k_x x + n\theta)}, x \in \quad, \theta \in [-\pi,\pi]$. One should bear in mind that the pressure field beneath a turbulent boundary can be characterized using realizations of uncorrelated wall plane waves [37]. Therefore, $\tilde{H}_p(x,\theta,r,k_x,n,\omega)$ in combination with $\tilde{\phi}_{pp}^{tbl}(k_x,n,\omega)$ is all what we need to get the ASD of the radiated pressure at the field point M. One way to calculate the circumferential sensitivity function of the shell consists in exciting its surface by wall plane waves with wavenumber couples (k_x,n). Unfortunately, that would result in a very lengthy procedure because the summation and integral of Eq. (6) involve a large number of couples. To avoid such a costly approach, a second interpretation of the sensitivity function can be considered, which relies on the Lyamshev reciprocity principle [21, 22] (see the illustration in Fig. 2). In the present situation, the principle states that the ratio between the acoustic pressure at point M and the radial point force applied at $\tilde{M}$ on the shell, namely $H_{p/F}$, equals the ratio of the radial velocity at point $\tilde{M}$ over the volume velocity at M, which we denote by H_{v/Q_v}. That is to say,

$$H_{p/F}(x,\theta,r,\tilde{x},\tilde{\theta},\omega) = H_{v/Q_v}(\tilde{x},\tilde{\theta},x,\theta,r,\omega). \tag{8}$$

Introducing Eq. (8) into Eq. (7) yields,

$$\tilde{H}_p(x,\theta,r,k_x,n,\omega) = \frac{R}{2\pi} \int_{-\infty}^{+\infty} \int_0^{2\pi} H_{v/Q_v}(\tilde{x},\tilde{\theta},x,\theta,r,\omega) e^{-jk_x\tilde{x}} e^{-jn\tilde{\theta}} d\tilde{\theta} d\tilde{x}. \tag{9}$$

From Eq. (9), a second interpretation of the circumferential sensitivity function is therefore possible. This function can now be viewed as the product of the radius R with the Fourier transform along x and the Fourier series decomposition along θ of the radial

velocity of the shell, when the shell is excited by an acoustic monopole of unit volume velocity located at $M(x,\theta,r)$. The advantage of this interpretation is that it allows one to obtain the circumferential sensitivity functions, for a large set of wavenumber couples (k_x,n), from a single computation involving the shell response to a monopole excitation at the field point $M(x,\theta,r)$. The radiated pressure at M due to the shell TBL excitation can then be obtained from Eq. (6), where the sensitivity functions are computed as a response to the monopole source at M and then multiplied with a CSD model for the TBL.

The next section is devoted to finding an analytical expression for the circumferential sensitivity functions for a periodically stiffened shell immersed in a fluid. Following the explanation above, our goal will be that of finding the radial velocity of the shell in the Fourier domain (k_x,n), when it is excited by a monopole source.

2.4 Circumferential sensitivity function for a submerged cylindrical shell with regularly spaced stiffeners

2.4.1 Mathematical problem formulation

The procedure that will be used to calculate the circumferential sensitivity function relies on the reciprocity principle, as manifested in Eq. (9), and is somewhat akin to previous formulations in literature (see e.g., [3,16,17]). Nonetheless, it still presents some significant differences with respect to those works. First, the shell excitation is due to a monopole source within the fluid. Second, the coupling between the shell and the stiffeners takes place through four DoF, namely the three translational directions plus the tangential angular rotation. Third and final, the dynamic behavior of the stiffeners is obtained from finite element models, which facilitates incorporating realistic designs for them.

Consider the infinite shell of Fig. 1 having thickness h, density ρ, Young modulus E, Poisson's coefficient ν and damping loss factor η. We denote by U, V and W the longitudinal (streamwise), tangential (circumference spanwise) and radial displacements of the shell, whereas Θ stands for the angular rotation (in the tangential direction). Θ is related to the radial displacement through $\Theta(x,\theta)=\dfrac{\partial W}{\partial x}(x,\theta)$. The shell stiffeners are regularly spaced along the x direction and separated apart a distance d. They are all identical with either rectangular or T-shaped cross sections and, as said, their dynamics are numerically modelled with the finite element method. The coupling between the thin shell

10

and each stiffener takes place alongside a circumference of the cylindrical neutral surface of the shell. The coupling is supposed to be rigid and involves the four DoF *U, V, W* and Θ. Additionally, let *L*, *T* and *F* respectively denote the longitudinal, tangential and radial loads the stiffeners apply on the shell. At each junction, we will impose continuity of the displacement fields between the stiffener and the shell, as well as force equilibrium.

The shell is immersed in an infinite fluid domain with density ρ_0 and speed of sound c_0 (note that no fluid is considered inside the shell), and it is excited by acoustic waves generated from a point monopole source within the fluid, located at $S(x_s, \theta_s, r_s)$.

To begin with, let us focus on how to obtain the shell displacements *U, V* and *W* (the coupling with Θ will be introduced at a later stage) as a response to the stiffener loads and the acoustic excitation. The latter will involve both, the incident waves from the monopole source and the acoustic waves radiated by the shell vibration. In what follows, a time dependence $e^{j\omega t}$ is assumed for all developments though it will be omitted in the notation.

The mathematical problem to be solved reads

$$
\{L_{3\times3}\}\begin{bmatrix} U(x,\theta) \\ V(x,\theta) \\ W(x,\theta) \end{bmatrix} = \gamma \left\{ \begin{bmatrix} 0 \\ 0 \\ -F_e(x,\theta) \end{bmatrix} + \begin{bmatrix} 0 \\ 0 \\ -p(x,\theta) \end{bmatrix} + \begin{bmatrix} L(x,\theta) \\ T(x,\theta) \\ F(x,\theta) \end{bmatrix} \right\},
\tag{10}
$$

where $\{L_{3\times3}\}$ stands for the Flügge equations of motion for a cylindrical shell (see e.g., [25]), and $\gamma = \dfrac{(1-\nu^2)R^2}{E^*h}$ with $E^* = E(1+j\eta)$ being the complex Young modulus.

The loads applied to the shell by the regularly spaced stiffeners can be decomposed as

$$
\begin{bmatrix} L(x,\theta) \\ T(x,\theta) \\ F(x,\theta) \end{bmatrix} = \sum_{m=-\infty}^{\infty} \begin{bmatrix} L_m(\theta)\delta(x-md) \\ T_m(\theta)\delta(x-md) \\ F_m(\theta)\delta(x-md) - M_m(\theta)\delta'(x-md) \end{bmatrix},
\tag{11}
$$

where L_m, T_m, F_m represent the longitudinal, tangential and radial line forces exerted by stiffener *m* on the shell, while M_m designates the tangential line moment exerted by such stiffener.

As for the acoustic monopole excitation of the shell, we shall split the total pressure in

11

the fluid domain, p_t, into the sum of the monopole blocked pressured F_e (i.e. the pressure generated by the monopole acoustic waves on the cylindrical shell as if that was rigid) and the pressure, *p,* radiated outwards by the shell vibrations. That is to say, $p_t = F_e + p$ [33]. The radiated pressure must satisfy, on the one hand, the homogeneous Helmholtz equation in the fluid medium,

$$\Delta p(x,\theta,r) + k_0^2 p(x,\theta,r) = 0,$$ (12)

where Δ is the Laplacian operator in cylindrical coordinates and $k_0 = \omega/c_0$ denotes, as usual, the acoustic wavenumber. If the free stream velocity U_0 was to be considered, one could solve the convected Helmholtz equation instead (see e.g., [34,35]). On the other hand, velocity continuity must be ensured between the shell motion and the fluid. The Euler equation allows to express that condition as

$$\frac{\partial p}{\partial r}(x,\theta,R) = \rho_0 \omega^2 W(x,\theta).$$ (13)

2.4.2 Resolution in the wavenumber domain

The solution to equations Eqs. (10) - (13) can be found by setting them in the wavenumber domain. Let us remind that, for a general field $f(x,\theta)$, its Fourier series decomposition along coordinate θ and the Fourier transform along *x* are given by

$$f(x,\theta) \mapsto \overline{f}(x,n) = \frac{1}{2\pi} \int_0^{2\pi} f(x,\theta) e^{-jn\theta} d\theta,$$
$$f(x,\theta) \mapsto \tilde{f}(k_x,n) = \frac{1}{2\pi} \int_{-\infty}^{+\infty} \int_0^{2\pi} f(x,\theta) e^{-j(k_x x + n\theta)} d\theta dx.$$ (14)

$\overline{f}$ and $\tilde{f}$ are respectively named the circumferential and the spectral fields of f. k_x is the space Fourier variable and *n* is the circumferential number. Note that the definitions in Eq. (14) are consistent with those in Eqs. (4)-(5) concerning the spectrum of the TBL wall pressure field, as well as with that in Eq. (9) involving the alternative interpretation of the circumferential sensitivity functions.

Applying Eq. (14) to Eq. (10), the equations of motion of the shell become

$$\left[\tilde{L}\left(k_x,n\right)\right]\begin{bmatrix}\tilde{U}\left(k_x,n\right)\\\tilde{V}\left(k_x,n\right)\\\tilde{W}\left(k_x,n\right)\end{bmatrix}=\gamma\left\{\begin{bmatrix}0\\0\\-\tilde{F}_e\left(k_x,n\right)\end{bmatrix}+\begin{bmatrix}0\\0\\-\tilde{p}\left(k_x,n\right)\end{bmatrix}+\begin{bmatrix}\tilde{L}\left(k_x,n\right)\\\tilde{T}\left(k_x,n\right)\\\tilde{F}\left(k_x,n\right)\end{bmatrix}\right\},\tag{15}$$

where $\begin{bmatrix}\tilde{L}\end{bmatrix}$ is the spectral Flügge matrix that depends analytically on the shell parameters

(see Appendix B). As regards the monopole source at $S\left(x_s,\theta_s,r_s\right)$, it generates a spectral

blocked pressure on the shell [33]

$$\tilde{F}_e(k_x,n)=\frac{j\omega\rho_0}{2\pi k_r R}\frac{H_n^{(2)}(k_r r_s)}{H_n^{(2)\prime}(k_r R)}e^{-j(n\theta_s+k_x x_s)},\tag{16}$$

where $H_n^{(2)}$ is the Hankel function of the second kind and order n, and

$$k_r=\begin{cases}\sqrt{{k_0}^2-{k_x}^2}&\text{if }\left|k_x\right|\le k_0,\\-j\sqrt{{k_x}^2-{k_0}^2}&\text{otherwise.}\end{cases}$$

Furthermore, the Fourier transform of Eqs. (12) and (13) permits relating the spectral

radiated pressure to the spectral radial displacement of the shell through the fluid

impedance, $\tilde{Z}_f$,

$$\tilde{p}(k_x,n)=j\omega\tilde{Z}_f(k_x,n)\tilde{W}(k_x,n),\quad\tilde{Z}_f(k_x,n)=-\frac{\rho_0 j\omega}{\overline{k}_r}\frac{H_n^{(2)}\left(k_r R\right)}{H_n^{(2)\prime}\left(k_r R\right)}.\tag{17}$$

Substituting Eq. (17) into Eq. (15) and inverting the matrix system provides the spectral

displacements of the shell,

$$\begin{bmatrix}\tilde{U}\left(k_x,n\right)\\\tilde{V}\left(k_x,n\right)\\\tilde{W}\left(k_x,n\right)\end{bmatrix}=\begin{bmatrix}\tilde{I}_{11}(k_x,n)&\tilde{I}_{12}(k_x,n)&\tilde{I}_{13}(k_x,n)\\\tilde{I}_{21}(k_x,n)&\tilde{I}_{22}(k_x,n)&\tilde{I}_{23}(k_x,n)\\\tilde{I}_{31}(k_x,n)&\tilde{I}_{32}(k_x,n)&\tilde{I}_{33}(k_x,n)\end{bmatrix}\left\{\begin{bmatrix}0\\0\\-\tilde{F}_e\left(k_x,n\right)\end{bmatrix}+\begin{bmatrix}\tilde{L}\left(k_x,n\right)\\\tilde{T}\left(k_x,n\right)\\\tilde{F}\left(k_x,n\right)\end{bmatrix}\right\},\tag{18}$$

where $\tilde{I}_{ij}$, $i\in\{1,2,3\}$, $j\in\{1,2,3\}$ correspond to the entries of the inverse of the Flügge matrix

taking the fluid impedance into account.

For properly resolving the coupling with the ring stiffeners, we should next introduce

the angular rotation in the formulation. In the wavenumber space, the spectral angular rotation

is related to the spectral radial displacement by $\tilde{\Theta}(k_x,n)=jk_x\tilde{W}(k_x,n)$. One can then easily

13

express Eq. (18) in the matrix form,

$$\tilde{\mathbf{W}}\left(k_{x},n\right)=\tilde{\mathbf{I}}\left(k_{x},n\right)\left[\tilde{\mathbf{F}}_{\mathbf{e}}\left(k_{x},n\right)+\tilde{\mathbf{F}}\left(k_{x},n\right)\right], \tag{19}$$

where now,

- $\tilde{\mathbf{W}}\left(k_{x},n\right)=\begin{bmatrix} \tilde{U}\left(k_{x},n\right) \\ \tilde{V}\left(k_{x},n\right) \\ \tilde{W}\left(k_{x},n\right) \\ \tilde{\Theta}\left(k_{x},n\right) \end{bmatrix}$ stands for the spectral vector of the shell DoF,

- $\tilde{\mathbf{I}}\left(k_{x},n\right)=\begin{bmatrix} \tilde{I}_{11}(k_{x},n) & \tilde{I}_{12}(k_{x},n) & \tilde{I}_{13}(k_{x},n) & \tilde{I}_{13}(k_{x},n) \\ \tilde{I}_{21}(k_{x},n) & \tilde{I}_{22}(k_{x},n) & \tilde{I}_{23}(k_{x},n) & \tilde{I}_{23}(k_{x},n) \\ \tilde{I}_{31}(k_{x},n) & \tilde{I}_{32}(k_{x},n) & \tilde{I}_{33}(k_{x},n) & \tilde{I}_{33}(k_{x},n) \\ jk_{x}\tilde{I}_{31}(k_{x},n) & jk_{x}\tilde{I}_{32}(k_{x},n) & jk_{x}\tilde{I}_{33}(k_{x},n) & jk_{x}\tilde{I}_{33}(k_{x},n) \end{bmatrix}$ represents the spectral

admittance matrix of the fluid loaded shell,

- $\tilde{\mathbf{F}}_{\mathbf{e}}\left(k_{x},n\right)=\begin{bmatrix} 0 \\ 0 \\ -\tilde{F}_{e}\left(k_{x},n\right) \\ 0 \end{bmatrix}$ is the spectral force vector due the external monopole excitation

and

- $\tilde{\mathbf{F}}\left(k_{x},n\right)=\sum_{m=-\infty}^{\infty}\begin{bmatrix} \bar{L}_{m}\left(n\right) \\ \bar{T}_{m}\left(n\right) \\ \bar{F}_{m}\left(n\right) \\ -jk_{x}\bar{M}_{m}\left(n\right) \end{bmatrix}e^{-jk_{x}md}$ is the spectral force vector due to the stiffener loads.

For convenience, we may rewrite

$$\tilde{\mathbf{F}}\left(k_{x},n\right)=\sum_{m=-\infty}^{\infty}\mathbf{J}\left(k_{x}\right)\bar{\mathbf{F}}_{m}\left(n\right)e^{-jk_{x}md} \tag{20}$$

with $\mathbf{J}\left(k_{x}\right)=\begin{bmatrix} 1 & 0 & 0 & 0 \\ 0 & 1 & 0 & 0 \\ 0 & 0 & 1 & 0 \\ 0 & 0 & 0 & -jk_{x} \end{bmatrix}$ and $\bar{\mathbf{F}}_{m}\left(n\right)=\begin{bmatrix} \bar{L}_{m}\left(n\right) \\ \bar{T}_{m}\left(n\right) \\ \bar{F}_{m}\left(n\right) \\ \bar{M}_{m}\left(n\right) \end{bmatrix}$.

Next, consider a finite element model of a ring stiffener. Given that the stiffener is

14

axisymmetric, axisymmetric shell elements could be adopted for efficiency; yet this is not mandatory. Classical 2D shell elements may be used as well, with a 3D surface mesh for the web and flange in the case of a T-shaped cross-section stiffener. The finite element model allows one to numerically estimate the circumferential admittance matrix of the stiffener, say $\bar{\mathbf{Y}}$, which relates the circumferential applied forces at the foot of the stiffener, $\bar{\mathbf{F}}_m^r$, to its circumferential displacements, $\bar{\mathbf{W}}_m^r(n)$, namely,

$$\bar{\mathbf{W}}_m^r(n) = \bar{\mathbf{Y}}(n)\bar{\mathbf{F}}_m^r(n) \ , \tag{21}$$

with $\ \bar{\mathbf{W}}_m^r(n) = \begin{bmatrix} \bar{U}_m^r(n) \\ \bar{V}_m^r(n) \\ \bar{W}_m^r(n) \\ \bar{\theta}_m^r(n) \end{bmatrix}, \ \ \bar{\mathbf{F}}_m^r(n) = \begin{bmatrix} \bar{L}_m^r(n) \\ \bar{T}_m^r(n) \\ \bar{F}_m^r(n) \\ \bar{M}_m^r(n) \end{bmatrix} \ $ and

$$\bar{\mathbf{Y}}(n) = \begin{bmatrix} Y_{UL}(n) & Y_{UT}(n) & Y_{UF}(n) & Y_{UM}(n) \\ Y_{VL}(n) & Y_{VT}(n) & Y_{VF}(n) & Y_{VM}(n) \\ Y_{WL}(n) & Y_{WT}(n) & Y_{WF}(n) & Y_{WM}(n) \\ Y_{\theta L}(n) & Y_{\theta T}(n) & Y_{\theta F}(n) & Y_{\theta M}(n) \end{bmatrix}. \tag{22}$$

As said, the entries $Y_{\zeta\xi}$ of the circumferential admittance matrix Eq. (22), can directly be obtained from the finite element simulation as $Y_{\zeta\xi}(n) = \dfrac{\zeta(n)}{\xi(n)}$, where $\zeta(n)$ is the circumferential displacement in response e.g., to a unit circumferential line load $\xi(n)$.

Knowing $\bar{\mathbf{Y}}$ and enforcing displacement and rotation continuity at each m-th ($m \in$) shell-stiffener junction i.e., $\bar{\mathbf{W}}_m(n) = \bar{\mathbf{W}}_m^r(n)$, as well as force equilibrium, $\bar{\mathbf{F}}_m(n) + \bar{\mathbf{F}}_m^r(n) = 0$, Eq. (21) becomes

$$\bar{\mathbf{F}}_m(n) = -\bar{\mathbf{Z}}(n)\bar{\mathbf{W}}_m(n), \text{ with } \ \bar{\mathbf{Z}} = \bar{\mathbf{Y}}^{-1}. \tag{23}$$

Furthermore, taking the inverse Fourier transform of the spectral displacements and rotation for $x = md$ we get

15

$$\bar{\mathbf{W}}_m(n) = \begin{bmatrix} \bar{U}_m \\ \bar{V}_m \\ \bar{W}_m \\ \bar{\theta}_m \end{bmatrix} = \frac{1}{2\pi} \int_{-\infty}^{\infty} \begin{bmatrix} \tilde{U}(\tilde{k}_x, n) \\ \tilde{V}(\tilde{k}_x, n) \\ \tilde{W}(\tilde{k}_x, n) \\ \tilde{\theta}(\tilde{k}_x, n) \end{bmatrix} e^{j\tilde{k}_x md} d\tilde{k}_x. \tag{24}$$

Substituting Eq. (24) in Eq. (23) and then inserting the output in Eq. (20), provides, after making use of Poisson's formula,

$$\sum_{m=-\infty}^{\infty} e^{j(\tilde{k}_x - k_x)md} = \frac{2\pi}{d} \sum_{m=-\infty}^{\infty} \delta\left(\tilde{k}_x - k_x - \frac{2m\pi}{d}\right), \tag{25}$$

the following expression for the stiffeners' spectral force vector,

$$\tilde{\mathbf{F}}(k_x, n) = -\frac{1}{d} \mathbf{J}(k_x) \bar{\mathbf{Z}}(n) \sum_{m=-\infty}^{\infty} \tilde{\mathbf{W}}\left(k_x + \frac{2m\pi}{d}, n\right). \tag{26}$$

Using this result, the spectral displacement vector in Eq. (19) can be written as

$$\tilde{\mathbf{W}}(k_x, n) = \tilde{\bar{\mathbf{I}}}(k_x, n)\left[\tilde{\mathbf{F}}_{\mathbf{e}}(k_x, n) - \frac{1}{d} \bar{\mathbf{Z}}(n) \tilde{\xi}(k_x, n)\right], \tag{27}$$

with $\tilde{\xi}(k_x, n) = \sum_{m=-\infty}^{\infty} \tilde{\mathbf{W}}\left(k_x + \frac{2m\pi}{d}, n\right)$ and

$$\tilde{\bar{\mathbf{I}}}(k_x, n) = \tilde{\mathbf{I}}(k_x, n)\tilde{\mathbf{J}}(k_x) = \begin{bmatrix} I_{11}(k_x, n) & I_{12}(k_x, n) & I_{13}(k_x, n) & -jk_x I_{13}(k_x, n) \\ I_{21}(k_x, n) & I_{22}(k_x, n) & I_{23}(k_x, n) & -jk_x I_{23}(k_x, n) \\ I_{31}(k_x, n) & I_{32}(k_x, n) & I_{33}(k_x, n) & -jk_x I_{33}(k_x, n) \\ jk_x I_{31}(k_x, n) & jk_x I_{32}(k_x, n) & jk_x I_{33}(k_x, n) & k_x^2 I_{33}(k_x, n) \end{bmatrix}.$$

Given the periodicity of $\tilde{\xi}(k_x, n) = \tilde{\xi}\left(k_x + \frac{2m\pi}{d}, n\right), \forall m \in \mathbb{Z}$, and resorting to Eq. (27), it follows that

$$\begin{aligned} \tilde{\xi}(k_x, n) &= \sum_{m=-\infty}^{\infty} \tilde{\mathbf{W}}\left(k_x + \frac{2m\pi}{d}, n\right) \\ &= \sum_{m=-\infty}^{\infty} \tilde{\bar{\mathbf{I}}}\left(k_x + \frac{2m\pi}{d}, n\right)\left[\tilde{\mathbf{F}}_{\mathbf{e}}\left(k_x + \frac{2m\pi}{d}, n\right) - \frac{1}{d} \bar{\mathbf{Z}}(n)\tilde{\xi}\left(k_x + \frac{2m\pi}{d}, n\right)\right], \end{aligned} \tag{28}$$

from which one can deduce,

16

$$\tilde{\boldsymbol{\xi}}(k_x, n) = \tilde{\mathbf{T}}_0(k_x, n) - \tilde{\mathbf{S}}_0(k_x, n)\overline{\mathbf{Z}}(n)\tilde{\boldsymbol{\xi}}(k_x, n), \tag{29}$$

with

$$\tilde{\mathbf{T}}_0(k_x, n) = \sum_{m=-\infty}^{\infty} \tilde{\tilde{\mathbf{I}}}\left(k_x + \frac{2m\pi}{d}, n\right)\tilde{\mathbf{F}}_{\mathbf{e}}\left(k_x + \frac{2m\pi}{d}, n\right), \tag{30}$$

and

$$\tilde{\mathbf{S}}_0(k_x, n) = \frac{1}{d}\sum_{m=-\infty}^{\infty} \tilde{\tilde{\mathbf{I}}}\left(k_x + \frac{2m\pi}{d}, n\right). \tag{31}$$

Solving for $\tilde{\boldsymbol{\xi}}$ in Eq. (29) and inserting the result in Eq. (27) yields the spectral displacement-rotation vector we were looking for,

$$\tilde{\mathbf{W}}(k_x, n) = \tilde{\tilde{\mathbf{I}}}(k_x, n)\left[\tilde{\mathbf{F}}_{\mathbf{e}}(k_x, n) - \frac{1}{d}\left[\overline{\mathbf{Y}}(n) + \tilde{\mathbf{S}}_0(k_x, n)\right]^{-1}\tilde{\mathbf{T}}_0(k_x, n)\right]. \tag{32}$$

Finally, and according to the reciprocity principle in section 2.3, the circumferential sensitivity function in Eq. (9) can be directly obtained from the spectral radial displacement vector induced by the monopole located at $S(x_s, \theta_s, r_s)$. Taking the radial component of $\widetilde{\mathbf{W}}(k_x, n)$ in Eq. (32) we get,

$$\tilde{H}_p(x_s, \theta_s, r_s, k_x, n) = j\omega R\tilde{W}(k_x, n). \tag{33}$$

2.5 Implementation aspects

In the precedent sections 2.2 to 2.4, we have left some points unspecified for the benefit of a more general formulation. In this section we will address them to make the simulations in the forthcoming sections reproducible.

Concerning the cross spectral density of the TBL, $\tilde{S}_{pp}^{tbl}(k_x, k_y, \omega)$, in Eq. (2) we have employed the model proposed by Chase [29]. From this model and Eq. (4) we can then compute the circumferential TBL excitation $\tilde{\phi}_{pp}^{tbl}(k_x, n, \omega)$. The Chase model requires the convective velocity, U_c (usually $U_c \approx 0.5U_0 - 0.7U_0$), the TBL thickness, δ_{tbl}, and the friction velocity, v_*, as input parameters. As the original model is a two-sided angular frequency spectrum, we have multiplied it by a factor 4π to convert it into a one-sided frequency spectrum. The Chase model is summarized in Appendix B for completeness of the paper.

Furthermore, and as mentioned before, Appendix B also contains an explicit expression for the spectral Flügge matrix in Eq. (15), $\left[\tilde{L}\right]$, which governs the dynamics of the shell and is crucial for all developments in section 2.4.2.

Another implementation aspect that is worth clarifying concerns the evaluation of infinite integrals and summations in some preceding expressions like Eq. (9), among many others. In practice, such developments must be truncated at some point. A criterion for doing so is as follows. For frequencies well above the hydrodynamic frequency, it is well known that the contribution of the convective peak is negligible to a good extent [36, 37]. Therefore, one can define an axial cut-off wavenumber $\bar{k}_x$ from the shell and fluid characteristics,

$$\bar{k}_x = \kappa_x \max\left(k_f, k_0\right),\tag{34}$$

where k_f is the flexural wavenumber of a plate equivalent to the shell (i.e. a plate with the same thickness and material than the shell), and k_0 is the acoustic wavenumber. The factor κ_x is a safety coefficient (typically $\kappa_x = 2$). Similarly, one can define a cut-off circumferential order, $\bar{N}$, as

$$\bar{N} = \mathrm{int}\left[\kappa_N R \max\left(k_f, k_0\right)\right] + 1,\tag{35}$$

where κ_N stands for a second safety coefficient that can be taken as $\kappa_N = 1.5$.

Once defined the threshold values Eq. (34) and Eq. (35), one can well estimate the main output of this work, namely the ASD function of the radiated pressure in Eq. (1) as,

$$S_{pp}\left(x, \theta, r, \omega\right) \approx 2\pi \sum_{n=-\bar{N}}^{n=\bar{N}} \int_{-\bar{k}_x}^{\bar{k}_x} \left|\tilde{H}_p\left(x, \theta, r, k_x, n, \omega\right)\right|^2 \tilde{\phi}_{pp}^{tbl}\left(k_x, n, \omega\right) dk_x.\tag{36}$$

The integral can be evaluated numerically using a quadrature rule.

On the other hand, infinite series summations also appear in the expressions for $\tilde{\mathbf{S}}_0$ and $\tilde{\mathbf{T}}_0$ (Eqs. (30) and (31)). Those can be approximated by truncating the summation over m between $-\bar{M}$ and $\bar{M}$, where $\bar{M}$ now stands for a cut-off stiffener number. A convergence study has revealed that $\bar{M}$ can be fixed to 15. Moreover, the inverse of the matrix $\bar{\mathbf{Y}} + \tilde{\mathbf{S}}_0$ in Eq. (32) can be calculated with the Cramer formula. Finally, the spectral displacement-rotation vector $\tilde{\mathbf{W}}(k_x, n)$ in Eq. (32) can be easily evaluated numerically.

As regard the computational cost, finite element model for the stiffeners apart, the

18

calculation of Eq. (36) can be performed on a standard PC (i.e. Intel Core i7-7500 2.7 GHz 8 GB RAM) using a Matlab code, which only takes a few seconds per frequency.

3. Numerical simulations and analysis of the results

The theoretical formulation is applied to analyze three different situations. The first one consists of a preliminary study in which we compare the ASD of the radiated pressure for an infinite panel under TBL excitation, with that of an infinite cylinder without supports. That will reveal the influence of curvature on the radiated sound pressure field. The other two cases are at the core of this paper and deal with submerged cylindrical shells with different types of periodic supports. Let us briefly survey the three configurations before starting the detailed analyses in the forthcoming subsections

Preliminary study: non-stiffened infinite panel versus non-stiffened infinite cylindrical shell. For a better comprehension and calibration of the numerical simulations, we begin computing the acceleration ASD on a flat plate excited by a TBL, for which experimental measurements exist (see [38]). To show that our theoretical model provides correct vibration values, we calculate the acoustic pressure ASD radiated by a fluid loaded cylindrical shell and compare it with that radiated by an infinite panel. For points in the near field, one should obtain very similar results, the influence of the shell curvature being minimal. As opposed, when moving away from the structure the differences between the plate and the shell should become apparent.

Case I: a submerged cylindrical shell with periodic simply supports. In this case we consider a fluid loaded cylindrical shell with regularly spaced simply supports. This simplification will allow us to analyze the effects of periodic stiffening without the influence of the deformable stiffener dynamics. In the present formulation this is akin to setting infinitely rigid stiffeners in the radial direction, while suppressing them in the other ones. To attain this effect, and prevent numerical instabilities, we have chosen the following values for the entries in the circumferential admittance matrix Eq. (22), $Y_{UL}(n) = Y_{VT}(n) = 1 \ \text{m}^2/\text{N}, \ Y_{\theta M}(n) = 1 \ \text{rad/N}, \ Y_{WF}(n) = 10^{-15} \text{m}^2/\text{N}$ and zero otherwise.

19

Case II: a submerged cylindrical shell with periodic deformable ring stiffeners. In this second case we include the dynamics of the deformable stiffeners in the simulations. Stiffeners with two different cross-sections are considered; a first one with rectangular cross section (I-shaped) and a second one with T-shaped cross section (see Fig. 3). As explained in section 2.4, the circumferential admittance matrix, $\overline{\mathbf{Y}}$, in Eq. (22) will be now estimated from a finite element model. The influence of the coupling between DoF will be studied.

We have used the same cylindrical shell for the preliminary test and cases I and II. It has a radius of R=5 m and a thickness of h=0.03 m. The shell is made of standard steel ($\rho = 7800$ kg/m^3, $E = 2.1 \times 10^{11}$ Pa, $\upsilon = 0.3$, $\eta = 0.02$) and is submerged in water ($\rho_0 = 1000$ kg/m^3, $c_0 = 1500$ m/s). The fundamental ring frequency of the cylindrical shell is 173 Hz. Likewise, we also use the same TBL excitation for all cases. The Chase model in Appendix B has been implemented with input parameters typical from naval applications corresponding to the measured data presented in [38], namely a flow speed of 5.3 m/s, a convection flow speed of 3.2 m/s, a friction velocity of 0.16 m/s and a 0.11 m TBL thickness. From the CSD of Chase's model, we have computed the circumferential TBL excitation $\tilde{\phi}_{pp}^{tbl}\left(k_x, n, \omega\right)$ taking into account the implementation aspects in section 2.5, and then computed the ASD in $\mathrm{Pa}^2/\mathrm{Hz}$ of the radiated pressure from Eq. (36).

The frequency range of analysis comprises from 100 Hz to 1000 Hz. It is well above the hydrodynamic coincidence frequency, which is lower than 1 Hz. Note that the contributions of the convective peak of the WPF can then be neglected because they would be strongly filtered by the structure [36, 37]. Additionally, in the low wavenumber domain (delimited by $\overline{k}_x$ and $\overline{N}$ in Eqs. (34) and (35)), the dB levels of the wall-pressure field CSD will not experience significant variations, except for values close to the origin (see e.g., Fig. 4a in [21]). Therefore, the CSD function of the WPF at the low wavenumber range can be well approximated as being constant, without substantially affecting the summation in Eq. (36). This indicates that the term most influencing the radiated pressure in Eq. (36) will be the modulus of the circumferential sensitivity function of the stiffened shell, $\left|\tilde{H}_p\right|$.

20

Finally, let us mention that the calculation process described in Sec. 2 has been validated numerically by comparison with results from the circumferential admittance approach in [25,41]. In appendix C, both methods are applied to case II with T-shaped stiffeners showing very good agreement.

3.1 Preliminary study: non-stiffened infinite panel versus non-stiffened infinite cylindrical shell

Let us start considering the acceleration ASD, $S_{\gamma\gamma}^{panel}$, of an infinite panel excited by a TBL, which is given by (see [23]),

$$S_{\gamma\gamma}^{panel}(z,\omega) = \frac{1}{4\pi^2} \int_{-\infty}^{+\infty}\int_{-\infty}^{+\infty} \left| \tilde{H}_{\gamma}^{panel}(k_x,k_y,\omega) \right|^2 S_{pp}^{tbl}(k_x,k_y,\omega) dk_x dk_y, \tag{37}$$

as well as the ASD of the radiated acoustic pressure, S_{pp}^{panel}, at a distance z from the panel, namely,

$$S_{pp}^{panel}(z,\omega) = \frac{1}{4\pi^2} \int_{-\infty}^{+\infty}\int_{-\infty}^{+\infty} \left| \tilde{H}_{p}^{panel}(z,k_x,k_y,\omega) \right|^2 S_{pp}^{tbl}(k_x,k_y,\omega) dk_x dk_y. \tag{38}$$

The acceleration and radiated pressure sensitivity functions of the panel, $\tilde{H}_{\gamma}^{panel}$ and $\tilde{H}_{p}^{panel}$, can be expressed in terms of its impedance, Z_p, and the fluid impedance, Z_a,

$$\tilde{H}_{\gamma}^{panel} = -\frac{\omega^2}{Z_p + Z_a}, \quad \tilde{H}_{p}^{panel} = \frac{Z_a e^{k_z z}}{Z_p + Z_a}, \tag{39}$$

with $Z_p = D_p^*\left(k_x^2 + k_y^2\right)^2 - \rho h_p \omega^2$ and $Z_a = \frac{\rho_0 \omega^2}{k_z}$. D_p^* and h_p respectively stand for the complex flexural dynamic stiffness and the thickness of the panel, while the wavenumber k_z becomes,

$$k_z = \begin{cases} i\sqrt{k_0^2 - k_x^2 - k_y^2}, & \text{if } \sqrt{k_x^2 + k_y^2} < k_0, \\ -\sqrt{k_x^2 + k_y^2 - k_0^2}, & \text{otherwise.} \end{cases} \tag{40}$$

A rectangular rule can be used for the numerical computation of the integrals in Eqs. (37) and (38), and similar criteria to those in section 2.5 can be applied for the truncation and discretization in the wavenumber space (k_x, k_y). Likewise, we have employed the Chase TBL model in the above formulas with the parameters described in the introduction of section 3.

21

An initial verification has been performed to check whether the theoretical model for the acceleration ASD in Eq. (37) provides reliable results. This is done through comparison with the ASD from the finite panel in [38], for which experimental data is available. That panel was made of Plexiglas with thickness of 3 mm. The following mechanical properties have been assumed for it: a mass density of 1190 kg/m^3, a Young modulus of 2000 MPa, a Poisson coefficient of 0.37 and a damping loss factor of 0.01. The acceleration ASD from Eq. (37) has been found to decrease monotonically from 5×10^{-4} m^{2}s^{-4}Hz^{-1} at 100 Hz to 1.6×10^{-5} m^{2}s^{-4}Hz^{-1} at 1 kHz and to coincide with the general tendency and order of magnitude of the numerical and experimental data from Fig. 18 in [38]. It is to be noted, however, that the results in [38] were obtained for a finite size panel of 0.58×0.2 m^2 so its modal behavior cannot be recovered with the infinite plate theory in Eq. (37).

The next step has consisted in computing the ASD of the radiated pressure for both, the cylindrical shell introduced at the beginning of section 3 and an infinite panel with the same material and thickness used for the shell. The pressure ASD for the shell has been obtained from Eq. (1) (following the procedure in section 2 but for an unstiffened shell) and that for the panel from Eq. (38). Predictions have been made at two distances from the shell and panel, namely at 0.1 m and 10 m, and presented in Fig. 4.

Close to the structure, at 0.1 m, one can observe from Fig. 4 that the levels of the radiated pressure are almost identical for the shell and the panel. This is logical since near the shell that will look almost flat, its curvature hardly affecting the radiated noise. Only a very small difference (~1 dB) can be appreciated below 200 Hz, which could be attributed to a slight influence of the shell curvature (the ring frequency is 173 Hz). For the two structures, the radiated pressure decreases ~25 dB between 100 Hz and 1 kHz. A calculation of the ASD of the panel acceleration with Eq. (37) also indicates a strong reduction of 10.8 dB between these 2 frequencies (from 31.6 dB at 100 Hz to 20.8 dB at 1 kHz, dB$_{ref}$ = 10^{-12} m^{-2}s^{-4}Hz^{-1}). This may be attributed (at least partly) to the decrease in the ASD of the TBL wall pressure, which can be obtained through integration of the CSD of Chase's wall pressure model. That experiences a 16 dB drop from 116 dB at 100 Hz to 110 dB at 1 kHz (dB$_{ref}$ = 10^{-12} Pa^{2}Hz^{-1}).

When we move away from the structure and set the observation point at 10 m, significant differences emerge between the shell and panel ASD radiated pressure (2 dB at 100 Hz and 6 dB at 1 kHz, see Fig. 4). The shell curvature now becomes critical. Note that once in the far field, the pressure radiated by the panel is not dependent on the distance

22

from the panel, this is because the panel was considered to be infinite. Conversely, the pressure radiated by the cylindrical shell will experience a $1/r$ decay law with distance. Further, it can be observed from Fig. 4 the radiated pressure increases between 100 Hz and 1 kHz when z=10 m, whereas it decreases when z=0.1 m. The reason for that behavior at the far field can be attributed to the radiation efficiency performance below the critical frequency, which is 7.6 kHz for the considered panel. In fact, it has already been shown that the radiation efficiency increases with frequency in that range for a point excited panel (see e.g., [39]). Although we are herein considering wall pressure fluctuations beneath a TBL, which cannot strictly be identified with point loads, it looks like a similar radiation mechanism operates in the far field. Despite of the acceleration ASD being lower at 1 kHz than at 100 Hz, the pressure radiated by the panel at 10 m is higher at 1 kHz than at 100 Hz because the radiation efficiency precisely increases between 100 Hz and 1 kHz. The same behavior is observed for the unstiffened cylindrical shell in Fig. 4.

Once finished this brief overview on some characteristics of the radiated sound by infinite plates and cylinders, let us next focus on the influence of adding periodic supports or ring stiffeners to the latter.

3.2 Case I: a submerged cylindrical shell with periodic simply supports

3.2.1 Spectrum of the radiated pressure from the shell

In Fig. 5 we show the ASD function of the radiated pressure at different distances z from the cylindrical shell taking a separation of $d = 1.35$ m between the simple supports. The receiver point is located at an axial distance of 0.45 m from one of them. The radiated pressure does not obviously depend on θ due to axisymmetry.

As observed in this figure, the spectrum is rather smooth and shows little variation with frequency when the observation point is close to the shell ($z = 0.01$ m). As opposed, when we move away from the shell the spectra start exhibiting several bumps. Additionally, note that beyond a certain distance the difference between spectrum levels gets constant. For instance, there is an 8.5 dB offset between the spectrum at z=10 m and that for z=100 m. This is consistent with a $1/r$ (with r=R+z) decay law of the pressure ASD function, which is characteristic of cylindrically propagating acoustic waves. Beyond z=10 m, one could then consider that the receiving point lies in the acoustic far field. It should be stressed that, herein, the definition of far field is not related to the size of the radiating structure, which is infinite, but to the shape of the wave fronts propagating in the fluid domain. For points closer to the shell than z=10 m, the far field behavior is not

23

observed at any frequency. For instance, the difference between the spectra at z=1 m and z=10 m has an almost constant value of 5.5 dB between 300 Hz and 1 kHz, which does not match with the cylindrical wave dependence $1/r$, because $10\log_{10}(15/6) \approx 4$. At frequencies lower than 300 Hz, the differences between the z=1 m and z=10 m spectra are no longer constant and clearly change with frequency. The evanescent waves radiated by the cylindrical shell play there a significant role. In what remains of this paper, however, we will mostly focus on the analysis of sound radiated to the far field.

Fig. 6 shows the radiated pressure spectra at a fixed distance z=10 m for different values of the support spacing d. For comparison, the pressure spectrum radiated from a cylindrical shell without supports is also plotted. As seen, the positions of the bumps and troughs in the spectra change with d. The larger the support spacing, the higher the number of bumps in the considered frequency range. Likewise, one notices that the regularly simply supported cylindrical shell radiates much more sound than the unsupported one. The differences are always higher than 12 dB and, at some frequencies, can even reach 32 dB.

The goal for the forthcoming sections is to better understand the physics behind the far field sound radiation of periodically simply supported shells, so as to provide an explanation for the results in Figs. 5 and 6. Three aspects will be investigated: (a) the contributions of the circumferential orders of the shell; (b) the role of the circumferential sensitivity functions; (c) the propagation of Bloch-Floquet waves in the shell.

3.2.2 Circumferential order analysis

Eq. (36) used to compute the far-field pressure radiation involves a summation over the 2 $\overline{N}$ +1 circumferential orders of the shell (from - $\overline{N}$ to $\overline{N}$). One can then separately study the individual contribution of the n-th order to the radiated pressure ASD. As the summation is over positive and negative values of n, we recognize the contribution of the n-th circumferential order, C_n, as that arising from the summation of the two terms with indices $-n$ and n in Eq. (36) (that is to say twice the term corresponding to n considering the symmetry about $\theta=0$). The n-th circumferential order contribution is then provided by,

$$C_n = 2\pi\varepsilon_n \int\limits_{-\bar{k}_x}^{\bar{k}_x} \left| \tilde{H}_p\left(x,\theta,r,k_x,n,\omega\right) \right|^2 \bar{\phi}_{pp}^{tbl}\left(k_x,n,\omega\right) dk_x,$$ (41)

24

with $\varepsilon_n = \begin{cases} 1 \text{ for } n = 0 \\ 2 \text{ for } n \in \ \overline{1, \bar{N}} \end{cases}$.

Fig. 7 shows some of the contributions of Eq. (41) to the radiated pressure at $z=10$ m for two situations: the regularly simply supported shell with $d=1.35$ m and the same cylindrical shell without supports. The contributions for $n=0$, $n=1$ and $n=5$ are respectively identified in the figure with full, dash-doted, and dashed lines, whereas additional results (for $2 \leq n \leq 4$ and $6 \leq n \leq 10$) are plotted with dotted lines without symbol distinction.

For the unsupported cylindrical shell (see Fig. 7a), the orders $n=0,1,2,3$ contribute similarly and much more than the remaining ones ($n \geq 5$), for the whole frequency range. As long as the circumferential order n increases, its low frequency contribution decreases, but recovers beyond a certain frequency value, which depends on n, reaching the contribution level of the first orders at high frequencies. The level of the radiated pressure by the cylindrical shell can then be roughly related to the number of orders achieving the levels of the first order contributions. For instance, at 100 Hz, only 4 circumferential orders have the top value contribution of 17 dB which results in an overall level of 22 dB. In contrast to that, at 600 Hz 11 orders have reached the top value of 14 dB giving an overall level of 24.8 dB. In summary, for the unsupported cylindrical shell the higher the frequency the larger the number of contributing circumferential orders, and the stronger becomes the radiated pressure at the far field.

The periodically simply supported shell exhibits some similitudes with the unsupported one: only the lowest orders (i.e. 1, 2) contribute to the radiated pressure for the whole frequency range (see Fig. 7b), yet most orders contribute to high frequencies. Nonetheless, a strong difference is observed. In the supported case, the circumferential order contributions present strong peaks and bumps depending on frequency. As observed in the figure, those peaks appear whatever the order n of C_n is, yet their amplitudes change from one order to the other. It is their cumulative effect what determines the overall radiated pressure level. Now, for better understanding the reason for the shape of the C_n contributions we shall analyse in detail the frequency dependence of the circumferential sensitivity functions, $\tilde{H}_p(x,\theta,r,k_x,n,\omega)$, in Eq. (41), given that, as said at the beginning of the section, the CSD, $\tilde{\phi}_{pp}^{tbl}(k_x,n,\omega)$, for the TBL can be taken as almost constant for the considered wavenumber range.

3.2.3 **Analysis of the circumferential sensitivity functions**

Circumferential sensitivity functions for the unsupported and simply supported cylindrical shells are respectively presented in Figs. 8 and 9 at two different frequencies. These were chosen to highlight how differently the periodically supported shell radiates depending on frequency. The first one, 229.6 Hz, corresponds to a trough of the radiated pressure spectrum (37 dB of S_{pp}), while the second one, 353.9 Hz, is on a bump of the spectrum (50 dB of S_{pp}) (see Fig. 6).

The figures present the dependence of each circumferential sensitivity function on its order n and wave number k_x, for distances z=0.1, 1 and 10 m from the shell (Figs. 8a-c and Figs. 9a-c). For the unsupported shell in Fig. 8a (i.e. z=0.1 m), the sensitivity functions exhibit the highest values for points located on a hemi-ellipse that corresponds to the quasi-flexural motions of the shell (when considering the fluid added mass). Indeed, if we compute the natural flexural wavenumber $k_{f,water}$ of an equivalent plate to the shell (i.e. a plate with the same thickness and material properties, see [25]) and plot the hemi-ellipse $E_{fl} = \left\{ \left(k_x, R\sqrt{k_{f,water}^2 - k_x^2} \right), k_x \in \left[-k_{f,water}, k_{f,water} \right] \right\}$ in Fig.8a (white dashed line), we observe a very a good agreement between E_{fl} and the hemi-ellipse of the maximum values of the sensitivity functions. Therefore, one could attribute with confidence the highest values of the latter to the propagation of quasi-flexural waves in the shell.

As the observation point moves away from the shell (Figs. 8b and c), the circumferential functions rapidly decrease, except for the lower circumferential orders. The ellipse of flexural motions is still visible for 229.6 Hz at z=1 m, but it completely disappears at z=10 m. It is neither perceptible at z=1 m nor at z=10 m for 353.9 Hz. The reason for that is the filtering effect of the acoustic medium. To check that, the spectral blocked pressure in Eq. (16) induced by the propagative waves generated by a monopole located at z=10 m has been plotted in Fig. 8d. There, we have also included the acoustic hemi-ellipse $E_{ac} = \left\{ \left(k_x, R\sqrt{k_0^2 - k_x^2} \right), k_x \in \left[-k_0, k_0 \right] \right\}$, where k_0 is the acoustic wavenumber.

As observed, the spectral blocked pressure is only important for axial wavenumbers and circumferential orders inside, or close to, the acoustic ellipse. Comparing Fig. 8d with Fig. 8c we may conclude that the same occurs for the circumferential sensitivity functions. Therefore, the latter axial wavenumber and circumferential order contributions can no

26

longer be attributed to the propagation of quasi-flexural waves propagating on the shell. Additionally, note that the values of the sensitivity functions inside the acoustic semi-ellipse are nearly constant and that the size of the ellipse grows with frequency (the one for 353.9 Hz is bigger than that at 22.6 Hz, see Fig. 8c). This may explain why more circumferential modes contribute to the far-field radiated pressure as the frequency increases, as observed in Fig. 7a for the unsupported shell.

The circumferential sensitivity functions for the periodically simply supported shell are very different from those of the unsupported one, see Fig. 9. For instance, in the near field, z=0.1 m (Fig. 9a), they exhibit the most significant values for the circumferential orders $n \in \llbracket 14,20 \rrbracket \cup \llbracket 28,29 \rrbracket$ at 229.6 Hz and $n \in \llbracket 0,13 \rrbracket \cup \llbracket 27,30 \rrbracket \cup \llbracket 36,37 \rrbracket$ at 353.9 Hz. When the point of observation steps away from the shell, the sensitivity functions decrease, except for the lower circumferential orders, as it happened with the unsupported shell. Here again, the filtering effect of the acoustic medium comes into play. Nonetheless, some remarkable differences can be identified. In Fig. 9c one can observe how, for z=10 m, the contributions remain notable not only for the axial wavenumbers and the circumferential orders inside the acoustic ellipse, but also for the ones corresponding to periodic copies of it (those are obtained through translating vectors $\dfrac{2\pi p}{d}\vec{i}_{k_x}, p \in \mathbb{Z}^{*}$, where $\vec{i}_{k_x}$ is the unit vector of the k_x axis). The acoustic ellipse and its periodic copies have been plotted as white solid lines in Fig. 9d. These copies can be clearly attributed to the periodicity of the supports. In fact, they result from the reacting forces at the supports, in response to the shell motions produced by acoustic wave excitation. Mathematically, the copies correspond to a discrete Fourier transform of the spatial field with the resolution of the support spacing, d. The transform yields a spectrum in the wavenumber space of period $\dfrac{2\pi}{d}$.

At the far field z=10 m, the acoustic filtering effect turns to be very efficient for the 229.6 Hz frequency but not so much for the 353.9 Hz one. Whereas the circumferential orders $n \in \llbracket 14,20 \rrbracket \cup \llbracket 28,29 \rrbracket$ of the former are completely swept away by the acoustic medium, significant contributions are still observed at 353.9 Hz for the low circumferential orders $n \in \llbracket 0,10 \rrbracket$ (though the higher order ones, $n \in \llbracket 11,13 \rrbracket \cup \llbracket 27,30 \rrbracket \cup \llbracket 36,37 \rrbracket$ get eliminated). Those low circumferential orders noticeably contribute to the noise radiated at the far field. We should then identify which

type of waves in the shell are responsible for them. This is the goal of the next section.

3.2.4 **Propagative Bloch-Floquet waves**

It is a well-known fact that waves in periodically stiffened structures can be propagative for some frequency bands, referred to as *pass-bands*, while evanescent at others, the so-called frequency *stop-bands* [1, 3, 5]. These waves constitute a particular example of Bloch-Floquet's waves [40]. In our problem, they result from the complex interaction between the cylindrical shell motions and the periodically spaced supports. The frequency pass-bands and stop-bands can be predicted finding the roots of the dispersion equation associated to the considered system [1]. In general, the roots can be complex which leads to a tricky problem [3]. However, one can skip such difficulty by analyzing an equivalent conservative system without damping.

The damping of the periodically supported shell is of two types: (a) that related to the energy dissipated by the shell steel itself and (b) that arising from the radiation of acoustic waves into the fluid. To suppress the first one, we simply need to consider a real Young modulus instead of a complex one in the equations of motion of the shell. As for the second one, it suffices to take the real part of the fluid loading impedance $\tilde{Z}_f$ in Eq. (17). The free propagative waves of the Bloch-Floquet type in the supported shell read $\mathbf{W}(x,\theta) = \boldsymbol{\xi} e^{j\left(k_x^{BF} x + n^{BF}\theta\right)}, \boldsymbol{\xi} \in \mathbb{C}^4$ and are expected to be solutions of the conservative equations of motion of the system without external excitation. From Eq. (32), it is apparent that non-null solutions can only exist for couples $\left(k_x^{BF}, n^{BF}\right) \in \mathbb{C}^2$ satisfying the dispersion equation

$$\tilde{\Delta}\left(k_x^{BF}, n^{BF}\right) = \left|\overline{\mathbf{Y}}\left(n^{BF}\right) + \tilde{\mathbf{S}}_{\mathbf{0}}\left(k_x^{BF}, n^{BF}\right)\right| = 0. \tag{42}$$

The roots of Eq. (42) cannot be obtained explicitly and a numerical procedure is needed to find them. That is presented in Appendix D.

Fig. 10 shows the pass-bands and stop-bands for the periodically simply supported shell with $d=1.35$ m. For a fixed frequency and circumferential order n, a black point is plotted in the figure, whenever a couple $\left(\overline{k}_x^{BF}, n^{BF}\right)$ is found to correspond to a propagative Bloch-Floquet wave, according to the algorithm in Appendix D. Points being very close together appear like solid lines in the figure. These lines therefore identify the pass-bands of a given circumferential order. For instance, for $n=12$ one gets four

frequency pass-bands, namely [182.2 Hz-217.9 Hz], [347.8 Hz-411.2 Hz], [591.5 Hz-675.4 Hz] and frequencies beyond 917.1 Hz.

The algorithm in Appendix D is also capable of detecting the propagation of quasi-longitudinal and quasi-shear waves of the cylindrical shell. In Fig. 10 we have indicated the upper limit for shear wave propagation with a dashed line. Below that limit the propagation zone is almost global and there are no stop-bands. In that region it becomes difficult to make a distinction between the Bloch-Floquet waves and the quasi-longitudinal and quasi-shear ones (note that the latter cannot radiate significant noise). Nevertheless, one can extrapolate the behaviour of the Bloch-Floquet waves below the dashed line, from their behaviour above the line. At 229.6 Hz, one can appreciate two circumferential order pass-bands; the first one between orders 15 and 20 and the second for the order $n = 29$. As for 353.9 Hz, three circumferential order pass-bands exist. The first one ranges from 0 to 12, the second comprises the orders from 28 to 30 and the third corresponds to $n = 36$. These pass-bands match the circumferential orders with substantial contributions to the circumferential sensitivity functions for z=0.1 m, in Fig. 9a (see the discussion in Section 3.2.3). Therefore, the important near field contributions of the circumferential sensitivity functions for the supported shell in Fig. 9a which were absent for the unsupported shell in Fig. 8a, can be credited to propagative Bloch-Floquet waves.

It is to be noted that some Bloch-Floquet waves are not filtered by the acoustic medium and can also radiate in the far-field. To identify those which can radiate in the far-field, it suffices to consider the waves in the first Brillouin zone. In fact, those with coordinates $\left(\bar{k}_x^{BF}, n^{BF} \right)$ inside the acoustic ellipse will be able to do so. Analogously, a wave in the pth Brillouin zone with axial wavenumber $\bar{k}_x^{BF} + \dfrac{2\pi}{d} p$ will have coordinates $\left(\bar{k}_x^{BF} + \dfrac{2\pi}{d} p, n^{BF} \right)$ inside a periodic copy of the acoustic ellipse and therefore, it will be also capable to radiate to the far field.

In Fig. 11 we have plotted the values of $k = \sqrt{\left(\bar{k}_x^{BF} \right)^2 + \left(\dfrac{n^{BF}}{R} \right)^2}$, the Bloch-Floquet waves with $k \le k_0$ being those radiating outwards. The acoustic wavenumber k_0 is represented with a solid line in the figure. In addition, a dashed line has been used for k_l,

29

the wavenumber of the quasi-longitudinal waves, and a dash-dotted line for the wavenumber, k_s, of the quasi-shear ones. Waves with wavenumbers close to k_l or k_s are not of the Bloch-Floquet type and can be discarded for radiation into the far-field.

To facilitate comprehension, suitable Bloch-Floquet waves with $k \leq k_0$ have been highlighted in Fig. 11 with black circles in the frequency axis. For the circumferential order $n=1$ in Fig. 11a, one can identify four frequency bands: [168 Hz-171 Hz], [334 Hz – 425 Hz], [555 Hz – 711 Hz], and frequencies higher than 875 Hz. These bands correlate well with the bumps observed in Fig. 7b for $n=1$. The peak at the band [168 Hz-171 Hz] also appears in Fig. 7b for $n=5$ (yet it is 15 dB lower than that of $n=1$) though is not identified in Fig. 11b. However, the bands in black circles of Fig. 11b, namely [351 Hz – 416 Hz], [561 Hz – 707 Hz] and frequencies beyond 880 Hz, are slightly higher in frequency and narrower than those for $n=1$, and remain totally consistent with those in Fig. 7b. For a general overview of the situation, in Fig. 11c we have plotted the results for all circumferential orders between 0 and 70. The frequency bands for which $k \leq k_0$ is fulfilled can be easily identified and correlate well with the bumps observed in the radiated pressure spectra of Figs. 5 and 6.

Having reached this point, the following may be concluded about the pressure radiated by a fluid loaded shell, with periodic supports, excited by a TBL. The acoustic spectrum at the far-field is clearly higher than that of an unsupported shell, and exhibits several bumps and troughs, whose position and number depend on the spacing between supports. These bumps can be attributed to propagative Bloch-Floquet waves that barely suffer from acoustic filtering and thus radiate to the far field. If the periodic simply support condition were to be substituted by deformable ring stiffeners, the underlying physics will essentially remain the same though the dynamics of the stiffeners will somewhat influence the radiated spectrum. This will be analyzed in the next section.

3.3 Case II: a submerged cylindrical shell with periodic deformable ring stiffeners

Let us next consider the same shell as for case I but periodically stiffened with steel rings. Two stiffeners typical from naval applications will be analyzed. These are (see Fig. 3),

- I-shaped (i.e. rectangular) stiffeners with cross-section 200×25 mm^2;
- T-shaped stiffeners with cross-section $200 \times 15 / 200 \times 15$ mm^2.

As explained in Section 2.4.2, the circumferential admittance matrix $\overline{\mathbf{Y}}$ in Eq. (22) for each stiffener is estimated using the finite element method (FEM). As axisymmetric

shell elements are not available in every finite element code, we have employed 2D shell elements (see e.g., [41,42]) to simulate each part of the stiffener (e.g., the web and the flange of the T-shaped stiffener). The mesh has been chosen fine enough to ensure at least six elements per flexural wavelength at the highest frequency of interest. A direct analysis for harmonic excitation has been performed with the SDTools FEM code [43]. To excite all the circumferential orders in a single FEM calculation, we have successively applied a unit single point force in every direction (i.e. longitudinal, tangential, radial, tangential rotation) to the foot of the stiffener, for $\theta = 0$. Given that the stiffener is axisymmetric the circumferential orders are not coupled one to another. The circumferential admittances in every excited direction can then be deduced from a Fourier series decomposition of the FEM displacement response at the foot of the stiffener. The FEM computational cost remains small thanks to the geometry simplicity, and the Fourier factorization is easily achieved with a Matlab code.

Fig. 12 presents some circumferential admittances for the two considered stiffeners. The highest values correspond to the stiffener modes. We observe how for a given modal shape, the resonance frequency increases with the circumferential order. The resonance trajectories look quite similar for the tangential and radial forces, whatever the stiffener shape (see Figs. 12b and c). Yet some slight variations can be perceived indicating that the dynamic stiffnesses are not exactly the same for both stiffeners. In contrast, the trajectories for the axial force and the tangential momentum are completely different, which reveals that very different modal shapes are being excited in the two stiffeners.

To better illustrate these statements, in Fig. 13 we have sketched the shapes of the stiffeners' cross-sections at 1kHz corresponding to the circumferential orders of highest admittance values under axial and radial excitations, in Figs 12a and b. For the longitudinal excitation, the trajectories in Fig. 12a correspond to the cross-section mode shapes shown in Figs. 13a to c for the T-shaped stiffener, and to the shapes in Figs. 13e and f for the l-shaped stiffener. On the one hand, and as observed, for the l-shaped stiffener the cross-section of the two modes remains almost undeformed. The mode for n=36 corresponds to torsional motions of the beam-like stiffener whereas that for n=63 relates to flexural motions along the circumference. On the other hand, the cross-section and web of the three modes for the T-shaped stiffener becomes noticeably deformed, especially for n=24 and n=43.

For the radial excitation, the trajectories in Fig. 12c correspond to the cross-section modal shapes in Fig. 13d for the T-shaped stiffener, and to those in Fig. 13g for the

31

I-shaped stiffener. The cross-section of the latter and the web from the former remain almost undeformed and correspond to flexural motions along the shell circumference. This can explain why their trajectories are similar in Fig. 12c. Note that the flange of the T-shaped stiffener gets significantly distorted, but this part does not contribute meaningfully to the dynamic stiffness at this frequency.

Finally, it should be remarked that only the diagonal terms of the circumferential admittance matrix have been plotted in Fig. 12. Nonetheless, several off-diagonal entries of $\overline{\mathbf{Y}}$ (e.g., Y_{UM}, $Y_{\theta L}$, Y_{VF}, Y_{WT}) are non-null and shall be considered to predict the noise radiated by the stiffened shell.

3.3.1 **Influence of the stiffeners in the radial direction**

To better understand the role played by the stiffeners, a first set of calculations have been carried out assuming that the coupling between the shell and the stiffeners only takes place in the radial direction. To that purpose, we have considered the radial circumferential admittances $Y_{WF}(n)$ computed with FEM in Fig. 12c but imposed $Y_{UL}(n) = Y_{VT}(n) = 1$ m^2/N, $Y_{\theta M}(n) = 1$ rad/N and set the remaining admittances to zero. Therefore, the sole difference with the simply supported case analyzed in Section 3.2 comes from the values of the radial circumferential admittances Y_{WF}, which were set to 10^{-15} m^2/N in that case.

Fig. 14 compares the ASD functions of the radiated pressure at z=10 m for the periodically simply supported shell in Section 3.2, with those of shells with periodic I-shaped and T-shaped stiffeners. It is evident from the figure that allowing the stiffeners to deform in the radial direction has remarkable consequences on the radiated sound. The pressure levels are generally much lower than those of the simply supported shell. The latter can be considered as an asymptotic case of infinite rigidity in the radial direction. Softening the radial stiffness lowers the shell resistance to flexural motions, which reduces the noise radiation. Moreover, the location and shapes of the bumps and troughs substantially differ from those of the simply supported case. In contrast, the radiated pressure is very similar for the two stiffeners, the T-shaped stiffener producing slightly higher results than the I-shaped

32

one. This is in accordance with the similarities found for the radial admittances of the two stiffeners in Fig. 12c. A closer analysis of the first circumferential orders reveals that the radial admittances of the T-shaped stiffeners are, in general, slightly lower than those of the I-shaped stiffeners, which explains the differences in the radiated noise.

To gain further insight on the influence of the stiffeners on the radiated noise, in Fig. 15a we have plotted the contributions of the first circumferential orders for the shell with I-shaped stiffeners; the corresponding values of the radial circumferential admittances are given in Fig. 15b. One can compare the contributions in Fig. 15a with those for the simply supported case in Fig. 7b. As observed, the former are more complex and present stronger differences between orders than the latter. Likewise, note that the discrepancies between the figures are only due to the values assigned to the radial admittances. One can check how the latter influence the contributions to the pressure radiation by comparing Figs. 13a and b. Indeed, it is worthwhile noticing that: (a) for $n=0$, the lowest value of the contribution (12 dB) takes place at 169.1 Hz, which coincides with a maximum of the radial admittance magnitude; (b) for $n=1$ the contribution exhibits a local maximum at 169.1 Hz that corresponds to a minimum of the radial admittance; (c) for $n=2$ the contribution exhibits a local maximum at 339.9 Hz which again matches with a minimum of the radial admittance; (d), for $n=3$ we found a local maximum of the contribution at 512 Hz, pretty close to the minimum in the radial admittance at 509.1 Hz. Except for slight discrepancies at $n=3$, one can assert that for $n=0$, 1 and 2 local maxima in the contributions correlate well with peaks (or anti-peaks) in the radial admittances. When those reach their highest values (i.e. at resonances) the dynamic stiffness decreases and so does the radiated noise ($n=0$). As opposed, when the radial admittances achieve their lowest values (i.e. at anti-resonances) the stiffeners tend to block wave propagation, which strongly impacts the radiated noise ($n=1$, 2 and probably 3). One should recognize that the above analysis cannot give a full explanation for all observed variations in the circumferential order contributions. These are also instigated by the stiffness

33

mismatch between the shell and the stiffeners, as well as by the separation distance between the latter, as discussed in Section 3.2.4.

3.3.2 Influence of the coupling degrees of freedom

To finish the analysis of case II, a second set of calculations has been performed considering either two or four DoF at the junctions between shell and stiffeners, to complement the single DoF (radial) computation in the previous section. The radial displacement and angular rotation, which are related to flexural motions, are the ones selected for the two DoF simulations. The radial admittance Y_{WF} and the rotational admittance $Y_{\theta M}$ are computed from the FEM model whereas we set $Y_{UL}(n) = Y_{VT}(n) = 1$ m^2/N and null values for all other admittances. For the complete situation with four DoF, the full circumferential admittance matrix $\bar{\mathbf{Y}}$ in Eq. (22) is obtained from the FEM model and all diagonal and off-diagonal terms are taken into account.

Figs. 16a and b respectively present the radiated pressure ASD at the far field, when considering the T-shaped and I-shaped stiffeners. Each figure contains the results accounting for one (radial), two (radial plus tangential rotation) and four (three displacements plus rotation) DoF. If we first compare the plots for one and two DoF in Fig. 16a, we observe that the influence of the tangential rotation coupling is almost negligible for the T-shaped stiffener. Nonetheless, it is meaningful above 500 Hz for the I-shaped one (see Fig. 16b). Also, the importance of including all four DoF is clear from both figures. The first bump gets particularly affected. This may be related to the ring frequency of the shell, namely 173 Hz. Below, but close to that frequency, the longitudinal, shear and flexural motions of the cylindrical shell are strongly coupled due to the shell curvature. It is then necessary to include them all for a proper computation of the radiated pressure. As opposed, the coupling between shell motions weakens well above the ring frequency.

For an unstiffened cylindrical shell, its quasi-flexural motion is responsible for the radiated noise (under radial force excitations). At first sight, one would then expect that the two DoF coupling (related to the flexural motion) could suffice to describe the behavior of the stiffened shell (as commonly assumed in literature). Yet, the results in Fig. 16 reveal that this is not the case, especially for the shell with I-shaped stiffeners. The off-diagonal terms of $\overline{\mathbf{Y}}$ shall be therefore considered for a correct evaluation of the radiated pressure field.

4. Conclusions

A semi-analytical approach based on the wavenumber-point reciprocity principle to compute the vibroacoustic response of a periodically stiffened shell under a turbulent layer excitation has been proposed. The suggested method is efficient and easy to implement, and it requires the integration of the circumferential sensitivity functions over the wavenumber domain. An analytical expression of the circumferential sensitivity functions in the wavenumber space has been derived from the vibratory response of the shell excited by monopole source.

Two test cases have been examined, including the fluid-loaded shells excited by a TBL with regularly spaced simply supports and deformable ring stiffeners. For the latter case, a finite element model was used to estimate the circumferential admittances that characterize the dynamic behavior of the stiffener along the four degrees of freedom. To better understand the physics behind the far field sound radiation, the contributions of the circumferential orders of the shell to the radiated noise, as well as the effects of the pass-bands and stop-bands of Bloch-Floquet waves on the noise radiation have been studied. It has been observed that adding the stiffeners to the shell causes different behavior in the acoustic pressure response in the near field compared to the one in the far field. In particular, the inclusion of stiffeners increases noise radiation in the far field. The stiffener spacing as well as the dynamic stiffnesses of the ring stiffener along the different DOFs may influence the bumps in the noise spectrum at the far field. Moreover, the circumferential admittance approach [25, 41] makes it possible to extend the current work to study noise radiation of irregularly stiffened shells.

35

Acknowledgments

References

[1] D.J. Mead, Free wave propagation in periodically supported, infinite beams. J. Sound Vib. 11 (1970) 181-197.

[2] M.L. Rumerman, Vibration and wave propagation in ribbed plates. J Acoust Soc Am 57 (1975) 370–3.

[3] B. Mace, Periodically stiffened fluid-loaded plates, I: response to convected harmonic pressure and free wave propagation. J. Sound Vib. 73 (1980) 473–86.

[4] D. J. Mead, Wave propagation in continuous periodic structures: Research contributions from Southampton, 1964–1995. J. Sound Vib. 190(3), 495–524 (1996).

[5] D. J. Mead, Plates with regular stiffening in acoustic media: Vibration and radiation, J. Acoust. Soc. Am. 88 (1990) 391–401.

[6] J.H. Lee, and J. Kim, Analysis of sound transmission through periodically stiffened panels by space-harmonic expansion method. J. Sound Vib. 251 (2002) 349-366.

[7] B. Yuan, M. Chen, Y. Liu, S. Zhao, H. Jiang, Experimental and theoretical analysis for a fluid-loaded, simply supported plate covered by a damping and decoupling composite acoustic coating. Shock and Vib. ID 7460457 (2017) 1-12.

[8] T. Fu, Z. Chen, H. Yu, C. Li, X. Liu, An analytical study of the vibroacoustic response of a ribbed plate. Aerosp. Sci. Technol. 73 (2018): 96-104.

[9] D.J. Mead, N.S. Bardell, Free vibration of a thin cylindrical shell with periodic circumferential stiffeners. J Sound Vib. 115 (1987) 499–520.

[10] C. H. Hodges, J. Power, J. Woodhouse, The low frequency vibration of a ribbed cylinder. Part I: Theory, J. Sound Vib. 101 (1985) 219–235.

[11] C. H. Hodges, J. Power, J. Woodhouse, The low frequency vibration of a ribbed cylinder. Part II: Observations and interpretation, J. Sound Vib. 101 (1985) 237–256.

[12] C.B. Burroughs, Acoustic radiation from fluid-loaded infinite circular cylinders with doubly periodic ring supports, J. Acoust. Soc. Am. 75 (3) (1984) 715–722.

[13] J. Yan, T.Y. Li, T.G. Liu, J.X. Liu, Characteristics of the vibrational power flow

propagation in a submerged periodic ring-stiffened cylindrical shell, Appl. Acoust. 67 (2006) 550–569.

[14] J. Yan, T.Y. Li, T.G. Liu, J.X. Liu, X. Zhu, Space-Harmonic analysis of sound radiation from a submerged periodic ring-stiffened cylindrical shell. Appl. Acoust. 67 (2006) 743–55.

[15] Y. Tong, J. Fan, B. Wang, W. Tang, Vibroacoustic behavior of an infinitely long cylindrical shell with periodic internal lengthwise ribs. J. Acoust. Soc. Am 144 (3) (2018) 1528-1538.

[16] X. Cao, H. Hua, C. Ma, Acoustic radiation from shear deformable stiffened laminated cylindrical shells, J. Sound Vib. 331 (2012) 651-670.

[17] D. Tang, X. Yao, Y.Q. Jin, F.Z. Pa., Acoustic radiation from shear deformable ring-stiffened laminated composite cylindrical shell submerged in flowing fluid, Appl. Ocean Res., 61 (2016) 65-80.

[18] Flinovia – Flow induced noise and vibrations issues and aspects: A focus on measurement, modeling, simulation and reproduction of the flow excitation and flow induced response (Springer International Publishing Switzerland, 2015, pp. 357).

[19] Flinovia – Flow induced noise and vibrations issues and aspects II: A focus on measurement, modeling, simulation and reproduction of the flow excitation and flow induced response (Springer International Publishing Switzerland, 2019, pp. 344).

[20] Rumerman, M. L. Estimation of broadband acoustic power radiated from a turbulent boundary layer-driven reinforced finite plate section due to rib and boundary forces. J. Acoust. Soc. Am. 111 (2002) 1274-1279.

[21] L. Maxit, V. Denis, Prediction of flow induced sound and vibration of periodically stiffened plate, J. Acoust. Soc. Am. 133 (2013) 146-160.

[22] C. Marchetto, L. Maxit, O. Robin, A. Berry, Vibroacoustic response of panels under diffuse acoustic field excitation from sensitivity functions and reciprocity principles, J. Acoust. Soc. Am. 141 (2017) 4508–4521.

[23] C. Marchetto, L. Maxit, O. Robin, A. Berry, Experimental prediction of the vibration response of panels under a turbulent boundary layer excitation from sensitivity functions, J. Acoust. Soc. Am. 143 (2018) 2954-2964.

[24] L. Maxit, Wavenumber space and physical space responses of a periodically ribbed plate to a point drive: A discrete approach. Appl. Acoust. 70 (2009) 563-578

[25] L. Maxit, J.M. Ginoux, Sound radiated by a submerged irregularly ribbed shell: the circumferential admittance approach, J. Acoust. Soc. Am. 128 (2010) 137-151.

37

[26] C. Maury, P. Gardonio, S.J. Elliott, A wavenumber approach to modelling the response of a randomly excited panel. Part I: general theory, J. Sound Vib. 252 (2002) 83–113.

[27] G. M. Corcos, Resolution of pressure in Turbulence, J. Acoust. Soc. Am. 35 (1963) 192-199.

[28] M. C. Goody, Empirical spectral model of surface pressure fluctuations, AIAA J. 42 (2004) 1788–1794.

[29] D.M. Chase, The character of the turbulent wall pressure spectrum at subconvective wavenumbers and a suggested comprehensive model, J. Sound Vib. 112 (1987) 125-147.

[30] R.M. Lueptow, Turbulent boundary layer on a cylinder in axial flow, NUSC Technical Report 8389, Naval Underwarter Systems Center, USA, New London, September 1988. 62 p.

[31] Y. Li, Y. Zhang, D. Kennedy, Random vibration analysis of axially compressed cylindrical shells under turbulent boundary layer in a symplectic system. J. Sound Vib. 406 (2017) 161-180.

[32] C. Durant, G. Robert, P.J.T. Filippi, P.O. Mattei, Vibroacoustic response of a thin cylindrical shell excited by a turbulent internal flow: comparison between numerical prediction and experimentation, J. Sound Vib. 229 (2000) 1115–1155.

[33] J.H. James, Computation of Acoustic Power, Vibration Response and Acoustic pressures of fluid-filled pipes. Admiralty marine technology establishment, Teddington, England, AMTE report TM82036, 1982.

[34] M.S. Howe, Acoustics of fluid-structure interactions, Cambridge University Press, 1998.

[35] O.Guasch and R. Codina, An algebraic subgrid scale finite element method for the convected Helmholtz equation in two dimensions with applications in aeroacoustics, Comput Methods Appl Mech Eng., 196 (2007) 4672-4689.

[36] S. Hambric, Y. Hwang, W. Bonness, Vibrations of plates with clamped and free edges excited by low-speed turbulent boundary layer flow, J. Fluid Struct. 19 (2004) 93-110.

[37] L. Maxit, Simulation of the pressure field beneath a turbulent boundary layer using realizations of uncorrelated wall plane waves, J. Acoust. Soc. Am. 140 (2016) 1268-1285.

[38] E. Ciappi, F. Magionesi, S. De Rosa, F. Franco, Hydronynamic and hydroelastic

analyses of a plate excited by the turbulent boundary layer, J. Fluid Struct. 25 (2009) 321-342.

[39] J. Hannsen Su, R. Vasudevan, On the radiation efficiency of infinite plates subject to a point load in water, J. Sound Vib. 208 (1997) 441-445.

[40] D.M. Photiadis, J.A. Bucaro, B.H. Houston, Scattering from flexural waves on a ribbed cylindrical shell, J. Acoust. Soc. Am. 96 (1994) 2785-2790.

[41] V. Meyer, L. Maxit, J.-L. Guyader, T. Leissing, Prediction of the vibroacoustic behaviour of a submerged shell with non-axisymmetric internal substructures by a condensed transfer function method, J. Sound Vib. 360 (2016) 260-276.

[42] L. Maxit, Scattering model of a cylindrical shell with internal axisymmetric frames by using the Circumferential Admittance Approach, Appl. Acoust., 80 (2014) 10-22.

[43] Balmes E. Structural dynamics toolbox & FEMLink. User's guide (Sdtools, Paris, France, 2012. p. 696).

[44] Williams, E.G. Fourier acoustics: sound radiation and nearfield acoustical holography. Academic press, Elsevier, (1999).

Appendix A: TBL periodic cross spectral density functions in the spanwise direction

In order to make the spatial CSD of a TBL for flat surfaces, $S_{pp}^{tbl}(x, y, \omega)$, periodic along the shell circumference, $2\pi R$, we shall convolve it with a Dirac comb distribution to obtain,

$$\hat{S}_{pp}^{tbl}(x, y, \omega) \equiv S_{pp}^{tbl}(x, y, \omega) * \frac{1}{2\pi R} \mathrm{III}\left(\frac{y}{2\pi R}\right), \tag{1A}$$

where $\mathrm{III}\left(\dfrac{y}{2\pi R}\right) = 2\pi R \sum_{n=-\infty}^{+\infty} \delta(y - 2\pi R n)$ and $*$ denotes the convolution operator.

According to the Fourier transform properties of the convolution and of the Dirac comb (see e.g., [44], Eqs. (1.44)-(1.45)), the spatial Fourier transform of Eq. (1A) becomes,

$$\hat{\phi}_{pp}^{tbl}\left(k_x,k_y,\omega\right)=\int\limits_{-\infty}^{+\infty}\int\limits_{-\infty}^{+\infty}\hat{S}_{pp}^{tbl}\left(x,y,\omega\right)e^{-jk_xx}e^{-jk_yy}dxdy$$

$$=S_{pp}^{tbl}\left(k_x,k_y,\omega\right)\mathrm{III}\left(Ry\right)=\frac{1}{R}\sum_{n=-\infty}^{+\infty}\tilde{S}_{pp}^{tbl}\left(k_x,\frac{n}{R},\omega\right)\delta\left(k_y-\frac{n}{R}\right) \qquad (2A)$$

To avoid using distributions (like the Dirac comb) in the forthcoming expressions, we favour considering a Fourier series decomposition of the involved fields along the circumferential position. To that purpose, first note that the CSD function of the WPF in terms of the circumferential angle, $\phi_{pp}^{tbl}\left(x,\theta,\omega\right)$, is given by,

$$\phi_{pp}^{tbl}\left(x,\theta,\omega\right)=\hat{S}_{pp}^{tbl}\left(x,R\theta,\omega\right),\forall x\in\quad,\forall\theta\in\quad. \qquad (3A)$$

Writing $\hat{S}_{pp}^{tbl}\left(x,R\theta,\omega\right)$ as the inverse Fourier transform of $\hat{\phi}_{pp}^{tbl}\left(k_x,k_y,\omega\right)$ and using (3A) provides

$$\phi_{pp}^{tbl}\left(x,\theta,\omega\right)=\frac{1}{\left(2\pi\right)^2}\int\limits_{-\infty}^{+\infty}\int\limits_{-\infty}^{+\infty}\hat{\phi}_{pp}^{tbl}\left(k_x,k_y,\omega\right)e^{jk_xx}e^{jk_yR\theta}dk_xdk_y. \qquad (4A)$$

If we next introduce Eq. (2A) into Eq. (4A) we arrive at

$$\phi_{pp}^{tbl}\left(x,\theta,\omega\right)=\frac{1}{\left(2\pi\right)^2}\int\limits_{-\infty}^{+\infty}\int\limits_{-\infty}^{+\infty}\frac{1}{R}\sum_{n=-\infty}^{+\infty}\tilde{S}_{pp}^{tbl}\left(k_x,\frac{n}{R},\omega\right)\delta\left(k_y-\frac{n}{R}\right)e^{jk_xx}e^{jk_yR\theta}dk_xdk_y, \qquad (5A)$$

which may be simplified evaluating the integral over k_y,

$$\phi_{pp}^{tbl}\left(x,\theta,\omega\right)=\frac{1}{\left(2\pi\right)^2R}\sum_{n=-\infty}^{+\infty}\left\{\int\limits_{-\infty}^{+\infty}\tilde{S}_{pp}^{tbl}\left(k_x,\frac{n}{R},\omega\right)e^{jk_xx}dk_x\right\}e^{jn\theta}. \qquad (6A)$$

On the other hand, the CSD of the WPF in the $\left(k_x,n\right)$ space, namely $\tilde{\phi}_{pp}^{tbl}\left(k_x,n,\omega\right)$, corresponds to the Fourier transform of $\phi_{pp}^{tbl}\left(x,\theta,\omega\right)$ in the x direction and to its Fourier series decomposition in θ,

$$\tilde{\phi}_{pp}^{tbl}\left(k_x,n,\omega\right)=\frac{1}{2\pi}\int\limits_{-\infty}^{+\infty}\int\limits_{-\pi}^{\pi}\phi_{pp}^{tbl}\left(x,\theta,\omega\right)e^{-jk_xx}e^{-jn\theta}d\theta dx, \qquad (7A)$$

so that,

$$\phi_{pp}^{tbl}\left(x,\theta,\omega\right)=\frac{1}{2\pi}\sum_{n=-\infty}^{+\infty}\left\{\int\limits_{-\infty}^{+\infty}\tilde{\phi}_{pp}^{tbl}\left(k_x,n,\omega\right)e^{jk_xx}dk_x\right\}e^{jn\theta}, \qquad (8$$

A)

which is nothing but Eq. (5) in the main text. Eq. (4) in text follows from direct

40

comparison between Eq. (8A) and Eq. (6A).

Appendix B: TBL and shell models

The cross spectral density of the Chase TBL model is given by (see e.g., [28]),

$$\tilde{S}_{pp}^{tbl}\left(k_x,k_y,\omega\right)=\frac{\left(2\pi\right)^3\rho_0^{\,2}v_*^{\,3}}{\left[K_+^2+\left(b\delta_{tbl}\right)^{-2}\right]^{5/2}}\left\{C_M k_x^{\,2}+C_T K^2\left[\frac{K_+^2+\left(b\delta_{tbl}\right)^{-2}}{K^2+\left(b\delta_{tbl}\right)^{-2}}\right]\right\} \tag{1B}$$

with $K_+^2=\left(\omega-U_c k_x\right)^2\big/\left(hv_*\right)^2+K^2$, $K^2=k_x^{\,2}+k_y^{\,2}$ and recommended parameters $b\approx0.75$, $C_M\approx0.1553$, $C_T\approx0.0047$ and $h=3$ (see e.g., [34]). Note that a factor $\left(2\pi\right)^3$ has been added in Eq. (1B) if compared to Eq. (39) in [28], to account for the difference in the definition of the Fourier transform used in Chase's paper and in the present one (i.e., Eqs. (2)-(3)).

On the other hand, the spectral Flügge matrix $\tilde{L}\left(k_x,n\right)$ implemented in this work reads,

$$\tilde{L}\left(k_x,n\right)=\begin{bmatrix}\tilde{Z}_{UU} & \tilde{Z}_{UV} & \tilde{Z}_{UW}\\ \tilde{Z}_{UV}^* & \tilde{Z}_{VV} & \tilde{Z}_{VW}\\ \tilde{Z}_{UW}^* & \tilde{Z}_{VW}^* & \tilde{Z}_{WW}\end{bmatrix}, \tag{2B}$$

with

$$\tilde{Z}_{UU}=-R^2(k_l^2-k_x^2)+n^2\frac{1-\upsilon}{2}(1+\beta^2),\quad \tilde{Z}_{UV}=nR\frac{1+\upsilon}{2}k_x,$$

$$\tilde{Z}_{UW}=jk_x\left[-R\upsilon+\beta^2\left(-R^3k_x^2+n^2R\frac{1-\upsilon}{2}\right)\right],\quad \tilde{Z}_{VV}=R^2\frac{1-\upsilon}{2}k_x^2(1+3\beta^2)+n^2-R^2k_l^2,$$

$$\tilde{Z}_{VW}=-jn\left(1+\beta^2R^2\frac{3-\upsilon}{2}k_x^2\right),\quad \tilde{Z}_{WW}=1+\beta^2\left(R^4k_x^4+2n^2(R^2k_x^2-1)+n^4+1\right)-R^2k_l^2,$$

where $\beta=\dfrac{h}{R\sqrt{12}}$ and $k_l=\omega\sqrt{\dfrac{\rho(1-\upsilon^2)}{E}}$ is the wavenumber for compressional waves and the asterisk denotes the complex conjugate. Note that the Flügge equations in Eq. (10) have been written with a positive sign in front of the force terms *L, T, F* in the right hand side, to attain a Hermitian spectral Flügge matrix of the conservative system.

41

Appendix C: Numerical validation

To validate the semi-analytical approach proposed in Sec.2, we compared it with the circumferential admittance method (CAA) in [25, 41]. The latter relies on coupling the circumferential admittances of the fluid loaded cylindrical shell with the circumferential admittances of the ring stiffeners. The shell admittances were obtained using a spectral approach (see [25] for details), while those of the ring stiffeners were computed with the finite element method, as described at the beginning of Sec. 3.3. Once the admittance matrices were assembled, the circumferential coupling forces between the shell and the ring stiffeners were computed. Finally, the spectral velocity of the stiffened shell was calculated knowing these forces.

Case II introduced in Sec. 3 will be used for the purpose of validation. In that example, the shell ring stiffeners have a T-shaped cross section and a spacing of 1.35 m. The four DoFs in the connection between shell and stiffeners have been considered in all computations. It should be noted that in CAA calculations a finite number of ring stiffeners are used for the infinite shell, as opposed to our model in Sec. 2. To compensate this fact, and as illustrated in Fig. C.1, a large number of stiffeners (74) have been considered in the simulations. The observation point was chosen to be at x=0 m, which essentially corresponds to the middle of the stiffened section of the shell.

The CAA method was fully validated for radial point forces [25,41]. The CAA permits calculating the spectral radial displacement $\tilde{W}_F^{CAA}$ of the stiffened shell due to radial point force excitation at a given point (x_s, θ_s). Thanks to the wavenumber-reciprocity principle [21, 22], one can derive the acceleration circumferential sensitivity functions, $\tilde{H}_\gamma^{CAA}$ at the observation point from $\tilde{H}_\gamma^{CAA} = -R\omega^2 \tilde{\gamma}_F^{CAA}$.

On the other hand, the acceleration circumferential sensitivity functions can be also

42

computed with the analytical model of Sec. 2.4. For a radial point force excitation at (x_s, θ_s), the spectral blocked pressure on the shell is given by

$$\tilde{F}_e(k_x, n) = \frac{1}{2\pi} e^{-j(n\theta_s + k_x x_s)}, \tag{C.2}$$

instead of Eq. (16) which is valid for a monopole source. Considering this expression, Eq. (32) provides the spectral radial displacement of the shell, $\tilde{W}_F^{analytical}$, due to the point force excitation. The analytical expression of the acceleration circumferential sensitivity functions is then obtained as $\tilde{H}_\gamma^{analytical} = -R\omega^2 \tilde{W}_F^{analytical}$.

The comparison between the CAA ($\tilde{H}_\gamma^{CAA}$) and analytical $\left(\tilde{H}_\gamma^{analytical}\right)$ sensitivity functions is plotted in Fig. C.2. The results are shown for two frequencies. The first one, 285.8 Hz, corresponds to a frequency at which the shell strongly radiates to the far field, whereas for the second one, 512.0 Hz, the shell radiates very poorly (see Fig. 16 and Sec. 3.3.2). As observed in the figure, there is a very good agreement between the analytical and CAA results both in the amplitude levels and in the shape patterns in the (k_x, n) space. The highest contributions observed in the figure can be attributed to the propagative Bloch-Floquet waves.

Following the same procedure that lead us to Eq. (36), one can get an expression for the ASD of the shell radial acceleration excited by the TBL, in terms of the acceleration circumferential sensitivity functions, namely,

$$S_{\gamma\gamma}^\alpha(x_s, \theta_s, \omega) \approx 2\pi \sum_{n=-\bar{N}}^{n=\bar{N}} \int_{-\bar{k}_x}^{\bar{k}_x} \left| \tilde{H}_\gamma^\alpha(x_s, \theta_s, k_x, n, \omega) \right|^2 \tilde{\phi}_{pp}^{tbl}(k_x, n, \omega) dk_x. \tag{C.2}$$

with $\alpha \in \{\text{CAA, analytical}\}$.

The ASD radial acceleration dependence on frequency is plotted for both methods in Fig. C.3. Here again, one observes a very good agreement between the results from the proposed method in Sec. 2 and those of CAA. The small discrepancies in the figure may be

43

attributed to the fact that only a finite part of the infinite shell in the CAA model gets stiffened, while this is not the case for the analytical model.

Appendix D: Finding the roots of the dispersion relation for the Bloch-Floquet waves

A numerical procedure to find the roots of the dispersion relation Eq. (42) in text is as follows. First, however, let us notice two properties of the determinant function $\tilde{\Delta}\left(k_x^{BF}, n^{BF}\right)$ which are useful to restrict the computation interval of k_x^{BF}. These are,

(i)   The function $\tilde{\Delta}$ is $\dfrac{2\pi}{d}$ periodic in k_x, so the interval to find k_x^{BF} can be delimited to the so-called *first Brillouin zone,* $\left]-\dfrac{\pi}{d}, \dfrac{\pi}{d}\right]$,

(ii)   The function $\tilde{\Delta}$ is even in k_x, which allows one to further limit the computation interval to $\left[0, \dfrac{\pi}{d}\right]$.

Denote by $\bar{k}_x^{BF}$ the axial wavenumber of the Bloch-Floquet waves in the first positive Brillouin zone $\left[0, \dfrac{\pi}{d}\right]$. An infinite number of axial Bloch-Floquet wavenumbers k_x^{BF} can be deduced from $\bar{k}_x^{BF}$ and the properties of $\tilde{\Delta}$ described above.

In practice, the numerical procedure to find the couples $\left(\bar{k}_x^{BF}, n^{BF}\right)$ consists in searching, for each circumferential number $n \in \left[0, \bar{N}\right]$, the values of k_x that make $\tilde{\Delta}\left(k_x, n\right)$ vanish. The k_x values can be computed with a two-step algorithm. In the first step, the interval $\left[0, \dfrac{\pi}{d}\right]$ is discretized with a very fine resolution (10^{-4} m^{-1} in our case) to detect those k_x values at which $\tilde{\Delta}$ changes sign. These values are identified as $k_x^{+/-}$. In the second step we check whether the sign change at $k_x^{+/-}$ corresponds to a local minimum or maximum of $\left|\tilde{\Delta}\right|$, using a threshold criterion. Namely, if

$$\left|\tilde{\Delta}\left(k_x^{+/-}, n\right)\right| < 10^{-3} \left|\tilde{\Delta}\left(\frac{\pi}{d}, \bar{N}\right)\right| \quad \text{then} \quad \bar{k}_x^{BF} = k_x^{+/-} \quad \text{and} \quad n^{BF} = n.$$

$$\left|\tilde{\Delta}\left(k_x^{+/-}, n\right)\right| < 10^{-3} \left|\tilde{\Delta}\left(\frac{\pi}{d}, \bar{N}\right)\right| \quad \text{then} \quad \bar{k}_x^{BF} = $$
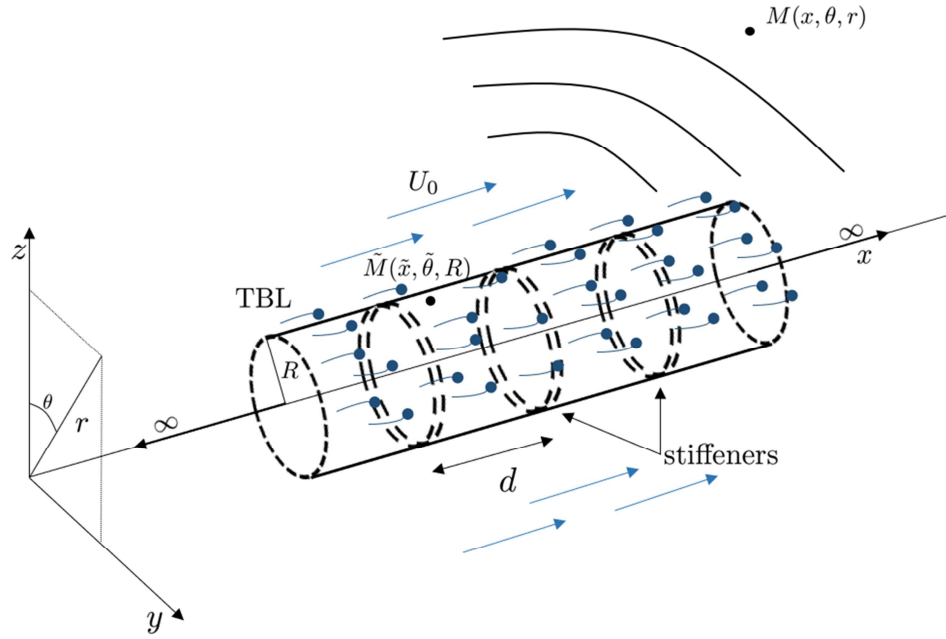
$$n^{BF} = n.$$

Figure captions

Figure 1. Periodically stiffened cylindrical shell immersed in a fluid and excited by a homogeneous stationary turbulent boundary layer.

Figure 2. Illustration of the Lyamshev reciprocity principle between structural and fluid domains.

Figure 3. Cross-sections of the two stiffeners considered in case II.

Figure 4. Comparison of the ASD function of the radiated pressure by the panel and the (unstiffened) cylindrical shell for two distances from the radiating structure: z=0.1 m and z=10

Figure 5. Case I: ASD function of the radiated pressure depending on the distance z to the shell for an observation point at an axial coordinate of 0.45 m. Separation between supports: $d = 1.35$ m.

Figure 6. Case I: ASD function of the radiated pressure at 10 m for various support spacing values, d. Comparison with the pressure radiated from non-supported shell.

Figure 7. Contributions of various n-th circumferential orders to the radiated pressure spectrum at z=10 m. (a) unsupported shell; (b) periodically simply supported shell with d=1.35 m.

Figure 8. (a)-(c), circumferential sensitivity functions of the unsupported shell in the (k_x,n) space for two frequencies: 229.6 Hz (left) and 353.9 Hz (right) and for three different distances to the shell: (a), z=0.1m. Hemi-ellipse associated to the flexural motion symbolized with a white dashed line (i.e. set of points $E_{fl} = \left\{ \left(k_x, R\sqrt{k_{f,water}^2 - k_x^2} \right), k_x \in \left[-k_{f,water}, k_{f,water} \right] \right\}$); (b), z=1 m; (c), z=10 m. (d), blocked

46

pressure induced by a monopole source located at a distance z=10 m from the shell. Hemi-ellipse associated to the acoustic propagation symbolized with a white solid line (i.e. set of points $E_{ac} = \left\{ \left(k_x, R\sqrt{k_0^2 - k_x^2} \right), k_x \in \left[-k_0, k_0 \right] \right\}$).

Figure 9. (a)-(c), circumferential sensitivity functions of the periodically simply supported shell with d=1.35 m in the (k_x,n) space for two frequencies: 229.6 Hz (left) and 353.9 Hz (right) and for three different distances to the shell: (a), z=0.1m; (b), z=1 m; (c), z=10 m. (d), acoustic ellipse and the periodic copies symbolized with white lines.

Figure 10. Pass-bands (lined) and stop-bands for each circumferential order depending on frequency. Periodically simply supported shell with d=1.35 m. The dashed line indicates the circumferential order bound of the propagative shear waves (i.e. $n_t = R\omega / c_t$ where c_t is the shear wave speed).

Figure 11. Values of the Bloch-Floquet wavenumbers of the first Brillouin zone depending on frequency for different circumferential orders. (a), n=1; (b), n=5; (c), $n \in [0, 70]$. Periodically simply supported shell with d=1.35 m. Solid line: k_0 (acoustic wavenumber); dashed line: k_l (longitudinal wavenumber); dash-dotted line: k_s (shear wavenumber).

Figure 12. Circumferential admittances of the stiffener with T-shaped cross section (left) and with I-shaped cross-section (right): (a), $10\log_{10}|Y_{UL}|$; (b), $10\log_{10}|Y_{VT}|$; (c), $10\log_{10}|Y_{WF}|$; (d), $10\log_{10}|Y_{\theta M}|$.

Figure 13. Shape (full line) of the stiffener cross-section at 1kHz for different circumferential orders N. Stiffener cross-sections: blue dashed lines; Deflection shape: continuous red lines. (a-d), T-shaped stiffener; (e-g), I-shaped stiffener; (a-c,e,f), axial excitation; (d,g), radial excitation.

Figure 14. ASD function of the radiated pressure at z=10 m for radial coupling between shell and stiffeners. Black solid line: periodic I-shaped stiffeners; dashed line: periodic T-shaped stiffeners; dotted line: simply supported conditions; Grey solid line: unstiffened shell. Results for d=1.35 m.

Figure 15. First fourth order contributions for the shell with I-shaped stiffeners (d=1.35 m). The shell and stiffeners are only assumed to be coupled in the radial direction (a) Radiated pressure contributions at z=10 m; (b) $10\log_{10}|Y_{WF}|$.

Figure 16. ASD function of the radiated pressure at z=10 m for the stiffened shell with d =1.35 m: (a) shell with T-shaped stiffeners; (b) shell with I-shaped stiffeners. Consideration of different coupling DoF. Dotted line: only radial coupling; dashed line: radial coupling force plus tangential coupling moment; Solid line: full coupling with four DoF. (i.e. three forces plus the tangential moment).

Figure C.1. Schematic representation of a mid-cut of the stiffened shell considered for the CAA model. The observation point M is located at x=0 m.

Figure C.2. Comparison of the acceleration circumferential sensitivity functions computed with the proposed analytical approach (a,c) and the CAA method (b,d). Results for frequencies: (a,b) 285.8 Hz; (c,d) 512.0 Hz.

Figure C.3. Comparison of the ASD function of the shell radial acceleration for the proposed semi-analytical method and the CAA simulation. Observation point M at x=0.

Figure 1. Periodically stiffened cylindrical shell immersed in a fluid and excited by a homogeneous stationary turbulent boundary layer.
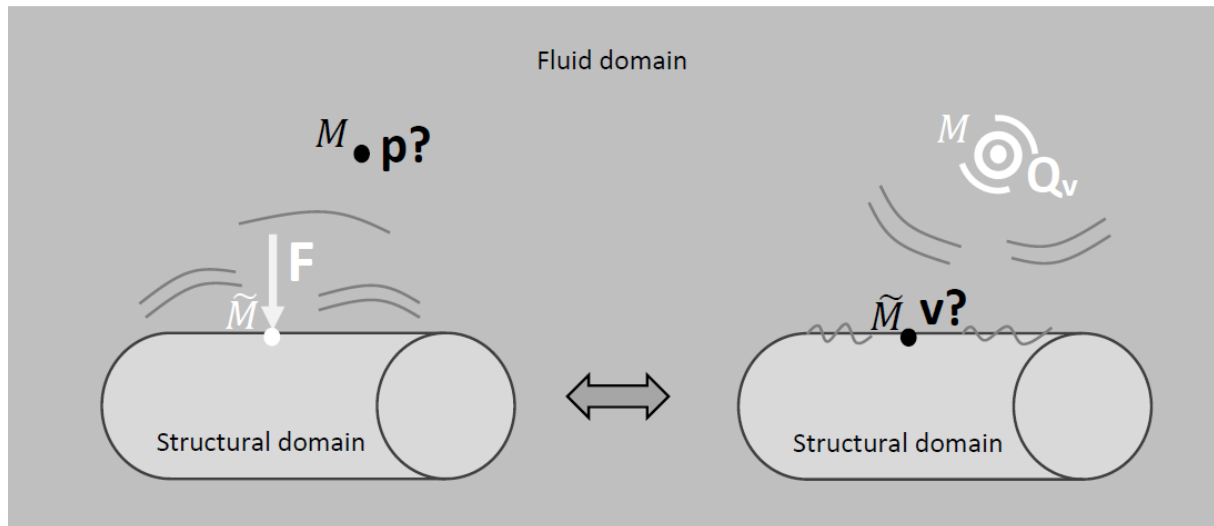
Figure 2. Illustration of the Lyamshev reciprocity principle between structural and fluid domains.
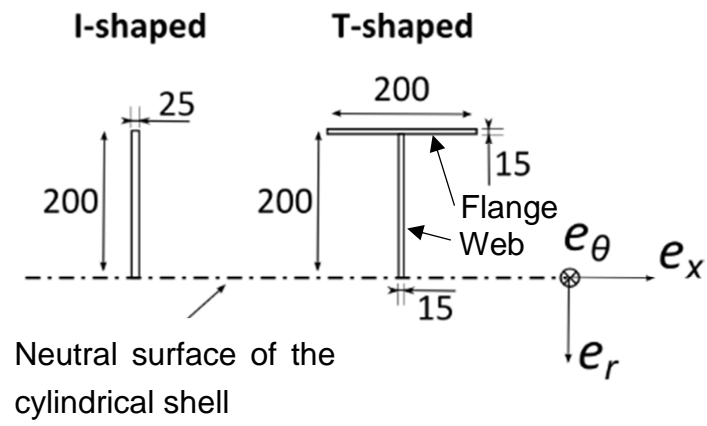
Figure 3. Cross-sections of the two stiffeners considered in case II.
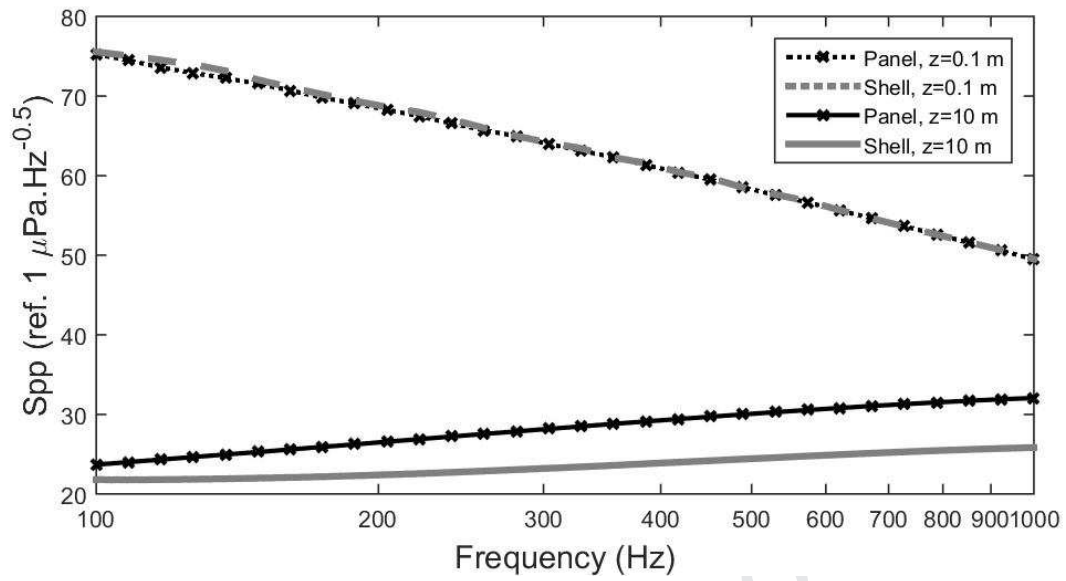
Figure 4. Comparison of the ASD function of the radiated pressure by the panel and the (unstiffened) cylindrical shell for two distances from the radiating structure: z=0.1 m and z=10 m.

Figure 5. Case I: ASD function of the radiated pressure depending on the distance *z* to the shell for an observation point at an axial coordinate of 0.45 m. Separation between supports: $d = 1.35$ m.

53

Figure 6. Case I: ASD function of the radiated pressure at 10 m for various support spacing values, *d*. Comparison with the pressure radiated from non-supported shell.

54

(a)

(b)

Figure 7. Contributions of various *n*-th circumferential orders to the radiated pressure spectrum at *z*=10 m. (a) unsupported shell; (b) periodically simply supported shell with *d*=1.35 m.

55

Figure 8. (a)-(c), circumferential sensitivity functions of the unsupported shell in the (k_x,n) space for two frequencies: 229.6 Hz (left) and 353.9 Hz (right) and for three different distances to the shell: (a), z=0.1m. Hemi-ellipse associated to the flexural motion symbolized with a white dashed line (i.e. set of points

$$E_{fl} = \left\{ \left(k_x, R\sqrt{k_{f,water}^2 - k_x^2} \right), k_x \in \left[-k_{f,water}, k_{f,water} \right] \right\} \text{);}$$
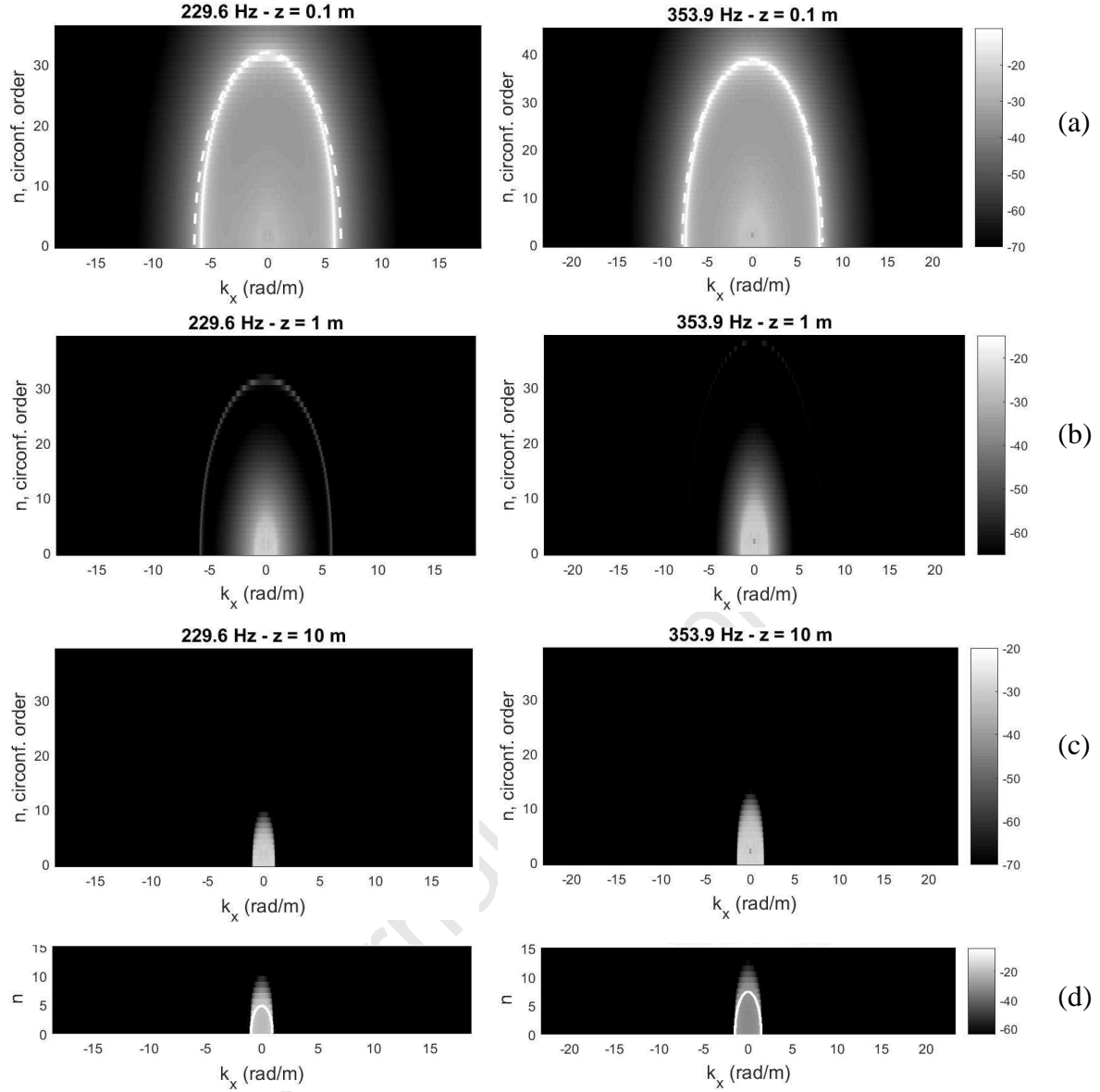
(b), z=1 m; (c), z=10 m. (d), blocked pressure induced by a monopole source located at a distance z=10 m from the shell. Hemi-ellipse associated to the acoustic propagation symbolized with a white solid line (i.e. set of points $E_{ac} = \left\{ \left(k_x, R\sqrt{k_0^2 - k_x^2} \right), k_x \in \left[-k_0, k_0 \right] \right\}$).

56

Figure 9. (a)-(c), circumferential sensitivity functions of the periodically simply supported shell with d=1.35 m in the (k_x,n) space for two frequencies: 229.6 Hz (left) and 353.9 Hz (right) and for three different distances to the shell: (a), z=0.1m; (b), z=1 m; (c), z=10 m. (d), acoustic ellipse and the periodic copies symbolized with white lines.

Figure 10. Pass-bands (lined) and stop-bands for each circumferential order depending on frequency. Periodically simply supported shell with d=1.35 m. The dashed line indicates the circumferential order bound of the propagative shear waves (i.e. $n_t = R\omega/c_t$ where c_t is the shear wave speed).

58

Figure 11. Values of the Bloch-Floquet wavenumbers of the first Brillouin zone depending on frequency for different circumferential orders. (a), n=1; (b), n=5; (c), $n \in [0, 70]$. Periodically simply supported shell with d=1.35 m. Solid line: k_0 (acoustic wavenumber); dashed line: k_l (longitudinal wavenumber); dash-dotted line: k_s (shear wavenumber).

59

Figure 12. Circumferential admittances of the stiffener with T-shaped cross section (left) and with I-shaped cross-section (right): (a), $10\log_{10}|Y_{UL}|$; (b), $10\log_{10}|Y_{VT}|$; (c), $10\log_{10}|Y_{WF}|$; (d), $10\log_{10}|Y_{\theta M}|$.

Figure 13. Shape (full line) of the stiffener cross-section at 1kHz for different circumferential orders *N*. Stiffener cross-sections: blue dashed lines; Deflection shape: continuous red lines. (a-d), T-shaped stiffener; (e-g), l-shaped stiffener; (a-c,e,f), axial excitation; (d,g), radial excitation.

Figure 14. ASD function of the radiated pressure at z=10 m for radial coupling between shell and stiffeners. Black solid line: periodic I-shaped stiffeners; dashed line: periodic T-shaped stiffeners; dotted line: simply supported conditions; Grey solid line: unstiffened shell. Results for d=1.35 m.
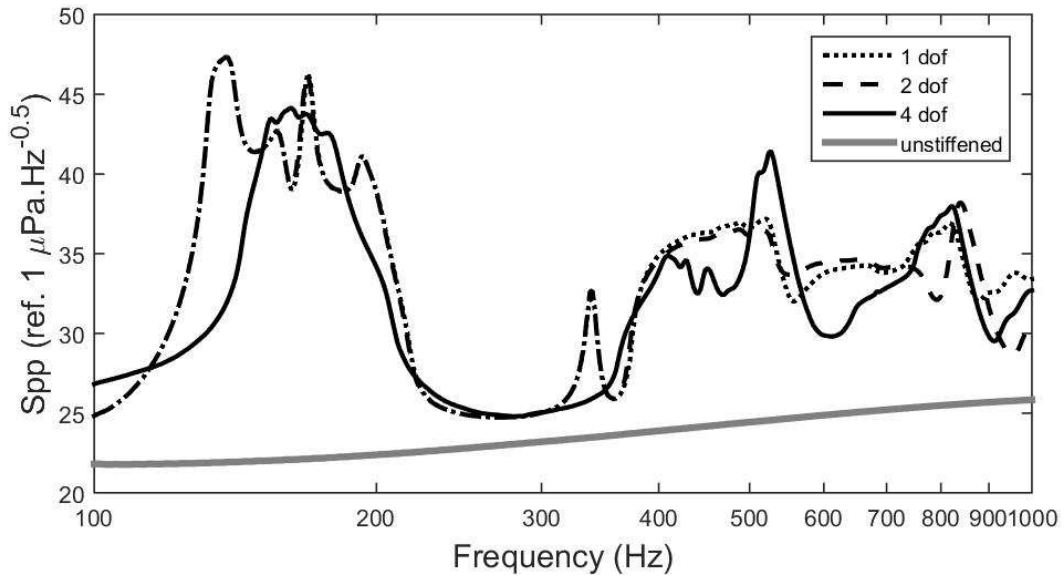
(a)

(b)

Figure 15. First fourth order contributions for the shell with I-shaped stiffeners (d=1.35 m). The shell and stiffeners are only assumed to be coupled in the radial direction (a) Radiated pressure contributions at z=10 m; (b) $10\log_{10}\left|Y_{WF}\right|$.

63

(a)

(b)

Figure 16. ASD function of the radiated pressure at z=10 m for the stiffened shell with d =1.35 m: (a) shell with T-shaped stiffeners; (b) shell with I-shaped stiffeners. Consideration of different coupling DoF. Dotted line: only radial coupling; dashed line: radial coupling force plus tangential coupling moment; Solid line: full coupling with four DoF. (i.e. three forces plus the tangential moment).
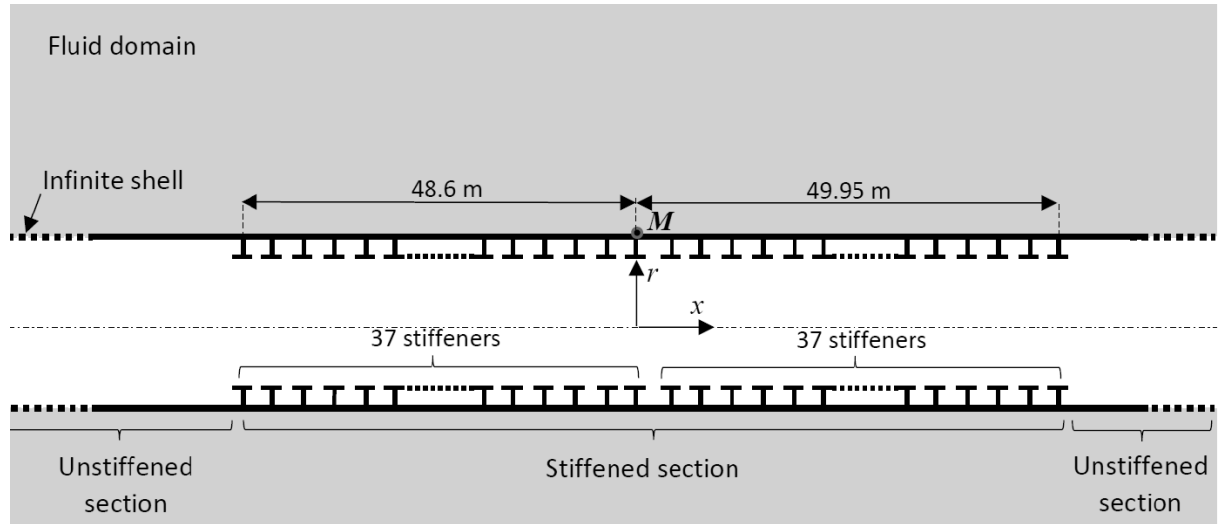
64

Figure C.1. Schematic representation of a mid-cut of the stiffened shell considered for the CAA model. The observation point M is located at x=0 m.
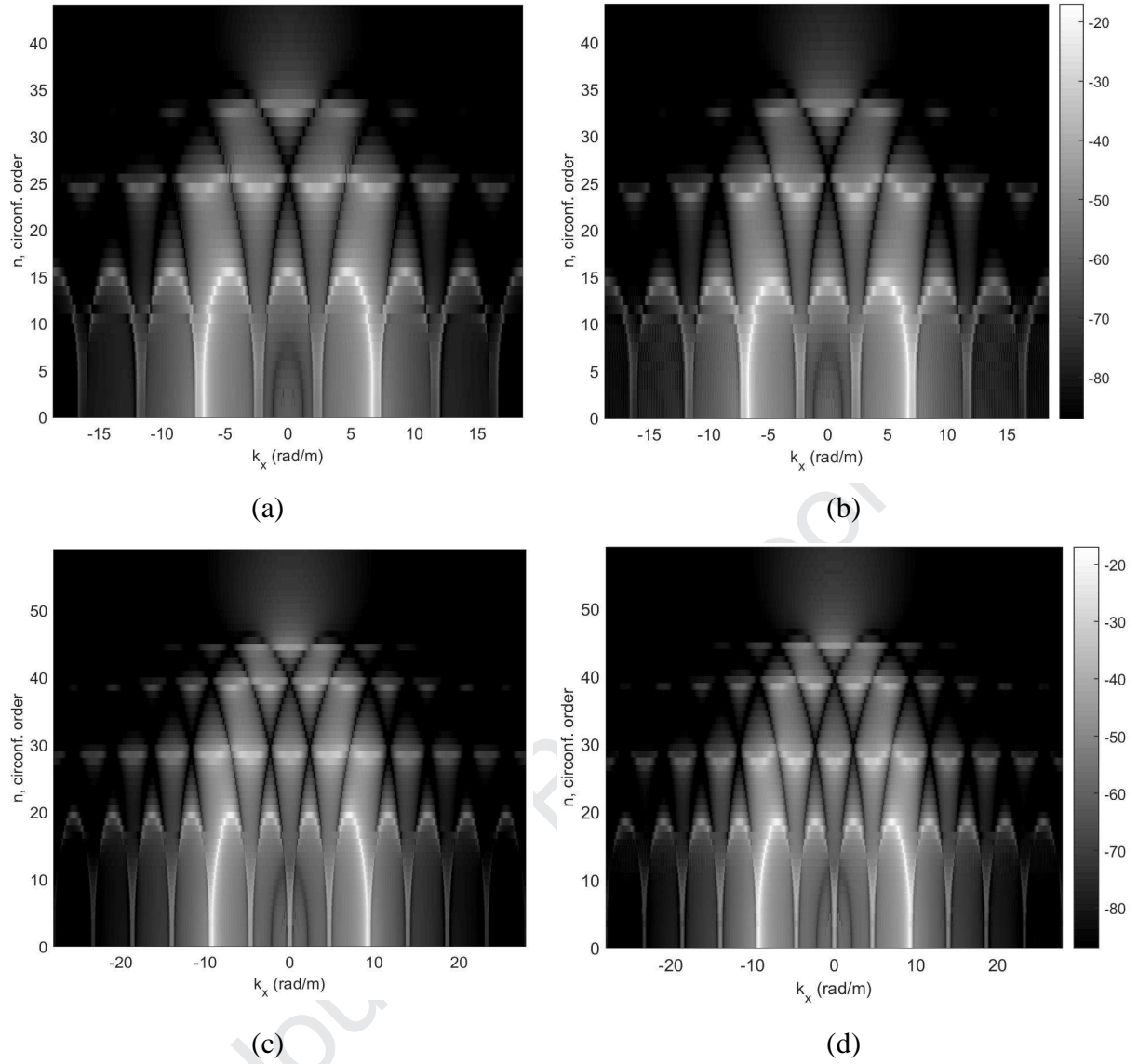
Figure C.2. Comparison of the acceleration circumferential sensitivity functions computed with the proposed analytical approach (a,c) and the CAA method (b,d). Results for frequencies: (a,b) 285.8 Hz; (c,d) 512.0 Hz.
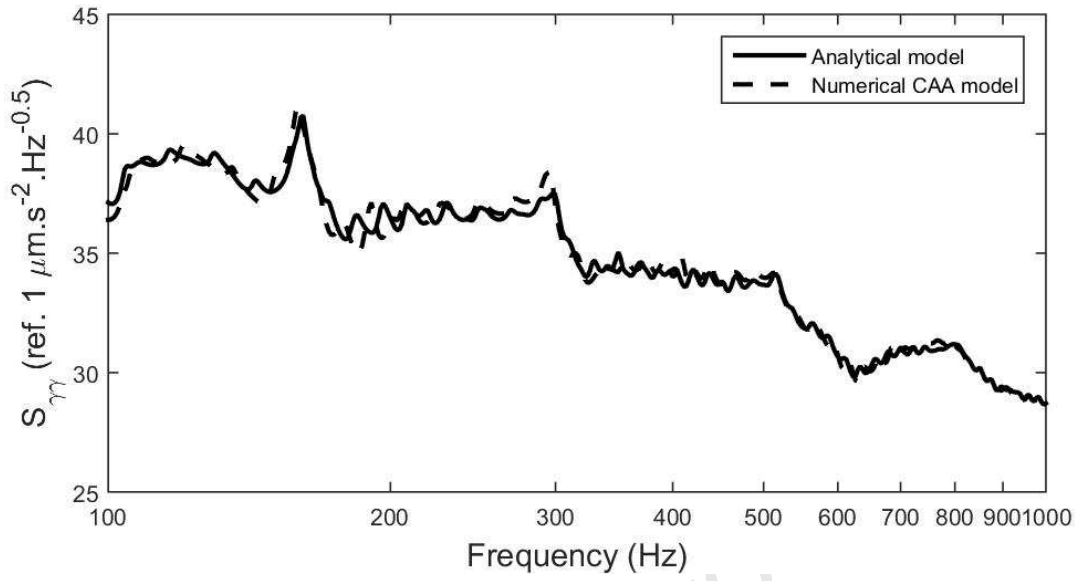
66

Figure C.3. Comparison of the ASD function of the shell radial acceleration for the proposed semi-analytical method and the CAA simulation. Observation point *M* at *x*=0.

Laurent MAXIT
Université de Lyon
INSA Lyon – Laboratoire Vibrations Acoustique
25bis avenue Jean Capelle
69621 Villeurbanne - France
+33 4 72 43 62 15
laurent.maxit@insa-lyon.fr

Lyon, 07/10/2019

Ref: JSV-D-19-00795
Title: Noise radiated from a periodically stiffened cylindrical shell excited by a turbulent boundary layer
Authors: Laurent Maxit, Oriol Guasch, Valentin Meyer, Mahmoud Karimi

Dear Prof. Lixi Huang,

The authors declare that they have no known competing financial interests or personal relationships that could have appeared to influence the work reported in this paper.

Sincerely yours,

On behalf of the authors, Laurent Maxit